



University of Kentucky  
UKnowledge

---

Theses and Dissertations--Mechanical  
Engineering

Mechanical Engineering

---


2021

## Modeling Thin Layers in Material Response Solvers

Christen Setters

*University of Kentucky*, [christen.setters@uky.edu](mailto:christen.setters@uky.edu)

Author ORCID Identifier:

 <https://orcid.org/0000-0003-2346-3713>

Digital Object Identifier: <https://doi.org/10.13023/etd.2021.404>

[Right click to open a feedback form in a new tab to let us know how this document benefits you.](#)

### Recommended Citation

Setters, Christen, "Modeling Thin Layers in Material Response Solvers" (2021). *Theses and Dissertations--Mechanical Engineering*. 183.

[https://uknowledge.uky.edu/me\\_etds/183](https://uknowledge.uky.edu/me_etds/183)

This Master's Thesis is brought to you for free and open access by the Mechanical Engineering at UKnowledge. It has been accepted for inclusion in Theses and Dissertations--Mechanical Engineering by an authorized administrator of UKnowledge. For more information, please contact [UKnowledge@lsv.uky.edu](mailto:UKnowledge@lsv.uky.edu).

## **STUDENT AGREEMENT:**

I represent that my thesis or dissertation and abstract are my original work. Proper attribution has been given to all outside sources. I understand that I am solely responsible for obtaining any needed copyright permissions. I have obtained needed written permission statement(s) from the owner(s) of each third-party copyrighted matter to be included in my work, allowing electronic distribution (if such use is not permitted by the fair use doctrine) which will be submitted to UKnowledge as Additional File.

I hereby grant to The University of Kentucky and its agents the irrevocable, non-exclusive, and royalty-free license to archive and make accessible my work in whole or in part in all forms of media, now or hereafter known. I agree that the document mentioned above may be made available immediately for worldwide access unless an embargo applies.

I retain all other ownership rights to the copyright of my work. I also retain the right to use in future works (such as articles or books) all or part of my work. I understand that I am free to register the copyright to my work.

## **REVIEW, APPROVAL AND ACCEPTANCE**

The document mentioned above has been reviewed and accepted by the student's advisor, on behalf of the advisory committee, and by the Director of Graduate Studies (DGS), on behalf of the program; we verify that this is the final, approved version of the student's thesis including all changes required by the advisory committee. The undersigned agree to abide by the statements above.

Christen Setters, Student

Dr. Alexandre Martin, Major Professor

Dr. Alexandre Martin, Director of Graduate Studies

Modeling Thin Layers in Material Response Solvers

---

DISSERTATION

---

A dissertation submitted in partial  
fulfillment of the requirements for  
the degree of Masters of Science in  
the College of Engineering at the  
University of Kentucky

By

Christen Setters

Lexington, Kentucky

Director: Alexandre Martin, Professor of Mechanical Engineering

Lexington, Kentucky

2021

Copyright© Christen Setters 2021

<https://orcid.org/0000-0003-2346-3713>

## ABSTRACT OF DISSERTATION

### Modeling Thin Layers in Material Response Solvers

Thermal Protection Systems (TPS) are a necessary component for atmospheric entry. Most TPS contain thin layers of various materials such as ceramic coatings, pore sealers and bonding agents. When modeling TPS, these thin layers are often neglected due to the difference in scale between the TPS (centimeters) and the thin layers (micrometers). In this study, a volume-averaging flux-conservation method is implemented in the governing equations of a finite volume material response code. The model proposes the addition of a volume and area fraction coefficient which utilizes a weighted-averaging between the amount of thin layer and heat shield material in a given cell. A verification case shows that the new model is capable of capturing physics of a thin layers of materials without additional computational costs. The model is also applied to heat conduction and porous flow to show that the volume-averaging flux-conservation model is effective at capturing the physics without adding additional computational cost.

KEYWORDS: Thin Layer, finite volume, ablation, thermal, material response

---

Christen Setters

---

November 24, 2021

Modeling Thin Layers in Material Response Solvers

By  
Christen Setters

Alexandre Martin

Advisor

Alexandre Martin

Director of Graduate Studies

November 24, 2021

Date

## ACKNOWLEDGMENTS

First I want to thank Dr. Alexandre Martin for all of his guidance as my research advisor. Thank you for taking the chance on me and help me learn how to conduct research as a scientist and engineer. Thank you to my committee members for their patience and insight.

I would like to acknowledge my mom, dad and brother for all of their support through out all these years. Thank you for doing everything possible to help me achieve my dreams. I would not have made it to this point in life without all the love and support. Thank you to my Godfather for encouraging me to go into STEM in the first place.

I want to thank my partner and other half, Gregory Walden. I know this has been a journey for both of us and I would not have been able to stay the course without your patience and constant support. Thank you for staying up late with me when I had assignments due so I was not staying up by myself. Thanks for constantly reminding me to smile and keeping me grounded. You have been my biggest cheerleader.

Last but certainly not least, I want to thank my lab mates, Ali, Justin, Olivia, Umran, Raghava and Ares for always being willing to lend a hand or an ear. A special shout out goes to Rui Fu for helping me learn the ropes and teaching me to take baby steps when it comes to research. Without you listening to all my crazy ideas and pushing me to think outside the box I would not have been able to make it as far as I have.

Dedicated to my grandparents (Lou and Flo Cavallaro).

## TABLE OF CONTENTS

Acknowledgments . . . . .	iii
List of Figures . . . . .	v
List of Tables . . . . .	ix
Chapter 1 Introduction . . . . .	1
1.1 Background . . . . .	1
1.2 Literature Review . . . . .	5
Chapter 2 Methodology & Verification . . . . .	15
2.1 Volume-Averaging Flux-Conservation Method . . . . .	15
2.2 Verification of the Model Using Energy Conservation . . . . .	17
2.3 Verification of Method on Flow through Porous Media . . . . .	28
Chapter 3 Heat Conduction . . . . .	35
3.1 One Dimensional Heat Conduction . . . . .	35
3.2 Two-Dimensional Heat Conduction . . . . .	36
Chapter 4 Material Response of Porous Charring Ablator . . . . .	42
4.1 One Dimensional Charring Ablator . . . . .	42
4.2 Two Dimensional Charring Ablator . . . . .	47
Chapter 5 Conclusion and Future Work . . . . .	54
Bibliography . . . . .	56



## LIST OF FIGURES

1.1	Graphic of the composition of the layers of material and interfaces that make up Thermal Barrier Coatings (TBC)s that protect turbine components. Reproduced with permission from [8]. . . . .	2
1.2	EBSD scan of a TBC system showing the layers of materials after the application of YSZ. Reproduced with permission from [24]. . . . .	8
1.3	SEM images of $\text{SiC}_3\text{N}_4$ coated steel substrate. Reproduced with permission from [27]. . . . .	10
1.4	Carton of the manufacturing process for rolled compacted UHTCMC fabrication. Reproduced with permission from [34] . . . . .	11
1.5	Cartoon of the ablation process and the different stages of the material. Reproduced with permission from [39] . . . . .	12
2.1	Hybrid cell containing bulk (green) and thin layer (light blue) materials. The fluxes on each side of the cell represent the exchange of conserved properties between the neighboring cells. . . . .	16
2.2	Computational mesh for a $25.4 \times 25.4 \text{ mm}^2$ block of material composed of solid metal with a thin layer of material on the surface with thickness $\varepsilon = 1.5875 \text{ mm}$ . . . . .	18
2.3	Temperatures extracted at cell centers when $\kappa$ was varied. . . . .	19
2.4	Cell center temperatures extracted for both domains when $\kappa$ was varied. . . . .	20
2.5	The total $\ L_2\ $ of shared cells as a function of time when $\kappa$ was varied. . . . .	21
2.6	Temperatures extracted at cell centers when $c_p$ was varied. . . . .	21
2.7	Cell center temperatures extracted for both domains when $c_p$ was varied. . . . .	22
2.8	The total $\ L_2\ $ of shared cells as a function of time when $c_p$ was varied. . . . .	23

2.9	Temperatures extracted at cell centers when $\rho$ was varied. . . . .	23
2.10	Cell center temperatures extracted for both domains when $\rho$ was varied.	24
2.11	The total $\ L_2\ $ of shared cells as a function of time when $\rho$ was varied. .	25
2.12	Temperatures extracted at cell centers from the volume-averaging flux-conservation domain with the two different thin layers thicknesses and material properties. . . . .	26
2.13	Cell center temperatures extracted for both test domains . . . . .	27
2.14	The total $\ L_2\ $ of shared cells as a function of time for $\zeta = 0.25$ and $\zeta = 0.50$ . . . . .	28
2.15	One dimensional domain with constant static pressure conditions used as the verification case for the pure flow. . . . .	28
2.16	Shows the solution is steady state expect for the near the thin layer. . . .	30
2.17	Results in (a) show parity between the thin layer and baseline pure flow case when comparing pressure. Temperature profiles in (b) show different profiles but the same gradient across the sample. The velocity profiles (c) show the same general trend in behavior. . . . .	31
2.18	Results in (a) show parity between the thin layer and baseline pure flow case when comparing pressure. Temperature profiles in (b) show different profiles but the same gradient across the sample. The velocity profiles (c) show the same general trend in behavior. . . . .	33
2.19	Results in (a) show parity between the thin layer and baseline pure flow case when comparing pressure. Temperature profiles in (b) show different profiles but the same gradient across the sample. The velocity profiles (c) show the same general trend in behavior. . . . .	34
3.1	Computational domain used for the 1D heat conduction case. The 25 mm bar was composed of 500 cells with uniform spacing. . . . .	35

3.2	Temperature profiles extracted along the z axis for the 1D heat conduction case for various thin layer locations. . . . .	36
3.3	Computational domain for 2D heat conduction cases. The $20 \times 10$ mm flat plate was composed of $80 \times 40$ cells with uniform spacing. . . . .	38
3.4	Temperature contour for the 2D flat plate . . . . .	38
3.5	The Gaussian distributions for the thin layer thickness, $\varepsilon$ , for the three different values of standard deviations. . . . .	39
3.6	Temperature contours for the 2D flat plate with a thin layer present at $x = 0.5$ mm with Gaussian distribution for $\varepsilon$ . . . . .	40
3.7	2D flat plate with a thin layer $x = 0.5$ mm where $\varepsilon$ was randomly assigned a value such that $0 \leq \varepsilon \leq .25$ mm where the average was $\varepsilon = 0.125$ mm. . . . .	40
4.1	Computational domain used for the 1D porous media case. The 100 mm bar was composed of 200 cells with non-uniform spacing . . . . .	42
4.2	Solution profiles for a 1D bar of TACOT material without a thin layer. . . . .	43
4.3	Solution profiles for a 1D bar of TACOT material with a thin layer at $z = 6.25$ mm. . . . .	44
4.4	Temperature profiles for a 1D bar of TACOT material with and without a thin layer at $t = 60$ s. . . . .	45
4.5	Velocity solution in the $z$ -direction for 1D bar of TACOT with and without a thin layer. . . . .	46
4.6	Pressure solutions for a 1D bar of TACOT with and without a thin layer at $t = 60$ s. . . . .	46
4.7	Solid density solutions for a 1D bar of TACOT material with and without a thin layer at $t = 60$ s. . . . .	47
4.8	Computational domain for the 2D flat plate porous media case. . . . .	48
4.9	Extracted at centerline $y = 5$ mm . . . . .	49

4.10	Temperature contours for baseline case without thin layer (top) and with a thin layer (bottom). . . . .	49
4.11	Pressure contours for baseline case without thin layer (top) and with a thin layer (bottom). . . . .	50
4.12	Solid density contours for baseline case without thin layer (top) and with a thin layer (bottom). . . . .	51
4.13	Comparison between baseline case and thin layer case. . . . .	52
4.14	Plotted streamtraces for the baseline and thin layer cases. . . . .	53

## LIST OF TABLES

2.1	Material properties for the $\kappa$ cerification case . . . . .	19
2.2	Material properties for $c_p$ verification case . . . . .	21
2.3	Material properties for $\rho$ verification case . . . . .	23
2.4	Material Properties for $\zeta = 0.25$ Verification Case . . . . .	26
2.5	Material Properties for $\zeta = 0.50$ Verification Case . . . . .	26
2.6	Porosity: Material properties for block in porous flow verification . . . . .	30
2.7	Permeability: Material Properties for block in Porous Flow Verification . . . . .	32
2.8	Porosity & Permeability: Material Properties for block in Porous Flow Verification . . . . .	32
3.1	Temperature difference between the case without a thin layer and cases with a thin layer . . . . .	37
4.1	Material Properties for thin layer for the Porous Flow Verification . . . . .	42

## Chapter 1 Introduction

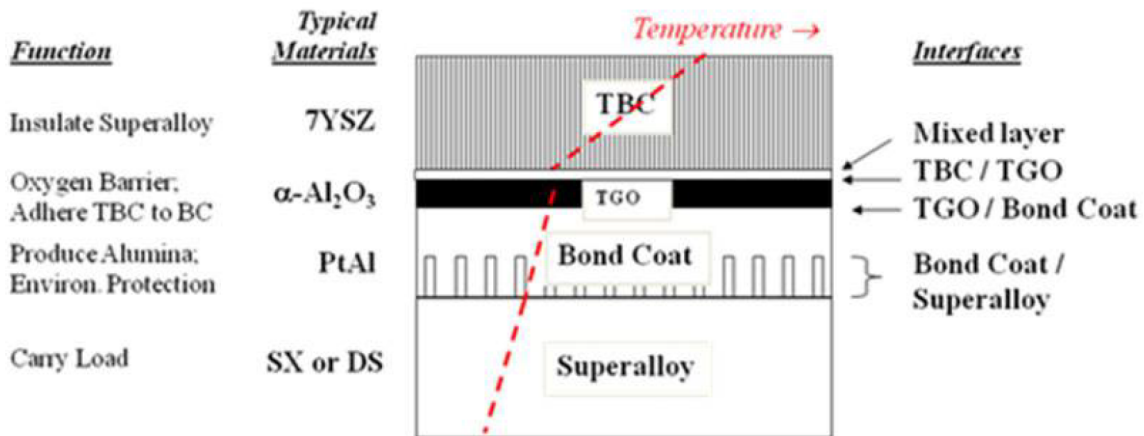
### 1.1 Background

Thin layers of materials are defined as compounds applied to a surface of a material that is at least several orders of magnitude thinner in thickness than the bulk material for which the compound was applied. Thin layers have a wide variety of applications spanning many industries. For example, in the automotive industry, thin films (on the order of  $\mu\text{m}$  thick) are used to make emission tracking more sensitive [1], to reduce vibration and interior cabin noise [2] and to protect paint from a variety of problems such as rust, chipping and weather resistance [2]. The textile industry uses thin layers to increase a materials ability to resist dirt and water without changing the inherent properties of materials such as softness, flexibility, and breathe-ability [3]. Medical grade joint replacements such as knees and hips as well as mechanical repairs to the heart and lungs require a thin coating material such as diamond-like carbon (DLC) in order to prevent wear once inside the body [4]. Pharmaceutical research is developing method of drug delivery using thin films [5]. This novel method speeds up the absorption of medication while making it easier for the patient to consume. Even if they can not be seen by the human eye, thin layers of materials are used all around us.

Thin layers are also applied to a multitude of surfaces (exposed surfaces, turbine blades, interior surfaces) within the aerospace industry, in order to handle a range of problems. Corrosion of structural components of an aircraft can lead to stress cracks and fatigue failures [6]. One way Boeing prevents corrosion from occurring is by applying “Corrosion Inhibiting Compounds (CIC)” during manufacturing [6]. Thin layers are applied to turbine fan blades in jet engines to extend the temperature

range of the blade before failure due to cyclic heat induced stress. These thin layers are often call Thermal Barrier Coatings (TBC) [7]. The complexity of these system is shown in Fig. 1.1. For decades, research has been conducted on to develop is

## TBC are Complex Multi-Layer Systems



### Complex Systems Tailored for Demanding Requirements:

- 4 material types and 4 interfaces; each with unique functions
- Each element has unique physical and mechanical properties
- Each component can have an effect on the other; all change with use
- **All materials / interfaces need to function together for performance reliability**

Figure 1.1: Graphic of the composition of the layers of material and interfaces that make up Thermal Barrier Coatings (TBC)s that protect turbine components. Reproduced with permission from [8].

the optimal chemical composition for a TBC, how to best apply the coatings and how long they last before they need coated or the part needs replaced [8]. Because most metals oxidize, ceramic thin layers called TBC are applied to metallic TPS to prevent oxidation from occurring [9]. Thin layers of materials have many usages for protecting structural materials in aerospace even extending to protecting them from extreme environments.

The materials used on vehicles that travel at hypersonics speeds are different than the rest of the aerospace industry. Traveling at such extreme speeds presents many

challenges, such as mitigation of the extreme heat generated through the interaction with the atmosphere. These special materials used to protect the vehicle from the atmospheric flow and large heat loads the main component of the Thermal Protection Systems (TPS). TPS are broken into two categories: passive TPS [10] and active TPS. Passive TPS are metal alloys designed to withstand the heat load. When hot structures are used on vehicles, several layers of insulation are placed between the passive TPS and the internal cavity. Passive TPS are often used on reusable vehicles and use materials such as Ultra High Temperature Ceramics (UHTC), Ceramic Matrix Composites (CMC) tiles, metallic tiles and insulators [11]. For example this type of TPS was used on space shuttle to protect the outer structure from heating due to radiation from the sun [10]. Active TPS fall into two different classifications; ablative (or active) or semi-passive [10, 12]. Ablative TPS consist of a single-use material that accommodates the high heat flux loads for a short duration of time [13]. Their main use is in extra-orbital atmospheric entry missions. The purpose of this TPS system is to convert the kinetic energy into chemical and thermal energy by using systems of mass transport such as erosion, spallation and chemical decomposition. This type of TPS was used during the Apollo missions [14], and include materials such as AVCOAT and PICA (Phenolic Impregnated Carbon Ablator) [11]. TPS are an essential part of traveling at hypersonic speed which are experienced when a vehicle enters an atmosphere during space travel.

A TPS is designed with two main purposes in mind. The first is to slow the vehicle down during atmospheric entry. The second is to protect the payload from the heat caused when entering an atmosphere or the heat caused by exposure to radiation from the sun when the vehicle is traveling through space [15]. The importance of a well designed TPS system was highlighted by Szirczak and Smith. They identified that TPS are a critical element for both hypersonic transport as well as space vehicles.



TPS plays a factor in the environment of the inside (protecting the payload whether it be scientific equipment or humans) of the vehicle and the ability for the structural integrity of the vehicle to withstand the thermal loads experienced at such speeds. In order to make hypersonic travel happen in the future, advanced testing techniques as well as advanced TPS materials need to be discovered. A more efficient method of testing these materials is to model their behavior. This will not remove all of the experimental testing that needs to be done, but modeling and simulation decreases the amount of experimental testing.

Thin layers of materials are present in most if not all types of TPS. For instance, ceramic thin layers called thermal barrier coatings (TBC) are applied to metallic TPS to prevent oxidation [9] at high temperatures. Carbon-carbon composites also oxidize at high temperatures. One method to solve the oxidation problem is to coat the C-C composite with a thin layer of a non-oxidizing material. There has been extensive experimental research conducted into the best coating material and application method. However, these experimental set ups are expensive to operate. Often times, the experiments conducted on TPS materials are destructive meaning the materials produce a large, expensive footprint in any project budget if experiments are the only source of data. These are also used for combining stacks of materials or tiles together to form larger blocks of materials or TPS.

Due to the scale difference between the thin layer ( $\mu\text{m}$ ) and the heat shield (cm) thickness, many challenge are present when trying to model the behavior of the thin layer. This scale differential requires the computational domain to be over resolved, thus increasing computational costs. In other words, the computational domain must be resolved down to the smallest scale, the thin layer. The present work proposed a homogenization method based on the flux decomposition occurring in a finite-volume scheme. The method is robust and efficient and does not significantly increase the

computational time. In the next chapter, the numerical framework for the volume-averaging flux-conservation method is described and is implemented using the thin layer volume and area fraction. A verification case is presented to show that the state-of-the-art approach and the volume-averaging flux conservation method proposed in this work produces the same results. Next, the verified model is applied to the governing equations in order to model the material response of a porous charring ablator.

## 1.2 Literature Review

Advanced TPS materials have become the focus for multiple studies in hypersonics due to the necessity of vehicles to go faster, be lighter, be durable and cost less. There has been research conducted on all types of TPS as well. Advanced TPS are made of a combination of materials and coating that as a system can withstand the wide array of conditions experienced when traveling at hypersonic speeds. There are three main materials that have the potential for these advanced TPS in the category of passive TPS: metallic structures, UHTC, and composites. These materials are being researched on their own and as combinations in order to make the best material with the ideal material properties. This work focused modeling the behavior of the thin layers under hypersonic conditions in order to further these existing materials as advanced TPS. The goal for this research is to further the capability of the modeling community to expand its search for materials by looking at thin layers as a possible solution for advanced TPS.

Metallic TPS were first introduced in the 1970s [16]. In the 1990s, NASA funded a program with Lockheed Martin to develop the X-33, which would have been a reusable launch vehicle (RVL). The X-33 program led to a decade of research into passive metallic TPS due to its desirable properties such as metals ability to retain shape

under thermal load while supporting the mechanical load on the vehicle [17]. Blosser et al [17] conducted a experimental study in 1998 to test different configurations of metallic TPS in various environmental conditions with a specific focus on their thermal and structural behaviors. The experiments conducted included water erosion, low speed impact tests, and high temperature impact testing in an arcjet [17]. They also developed an analytical model to demonstrate the low speed impacts. After the impact test was conducted on a panel, the sample was then tested in the arcjet. Some of these samples experienced spallation, breaking off of small chunks of material [18], of the oxidized material. This study tested both pre-oxidized and un-oxidized samples for fracture damage at angles of various angles of attack. The authors noted that both types of samples experienced cracking due to the impact of water droplets. The authors did not test different panels with thin layers of ceramics applied to the surface to experiment with preventing the damage to the metallic surface. The insulation for the metallic TPS being developed was constructed of thin ceramic composite foils which had a coating with high reflective properties. These foils were separated by insulation made from fibrous material. While the authors acknowledge the complexities of the heat transfer through multi-layer insulation materials, they only tested for effective thermal conductivity. A drawback of metallic TPS is that the metals are dense. Recall that the heavier a vehicle is, the more energy that is required to exit a gravitation force. This fact makes metallic TPS not a viable option for space travel outside of its reuse-ability and durability without the addition of thin layers of materials to extend its other properties.

UHTC are ceramics with melting points above  $2000^{\circ}\text{C}$ . During the space race in the 1950s and 1960s, there was a surge of interest from both nations involved to develop materials, such as UHTCs, that could withstand the extreme conditions of space travel and flight [19]. After the surge in the 1960s, research in UHTCs

dropped until the resurgence in hypersonic vehicle travel in the 1980s. This resurgence drove the need for materials to be able to withstand the extreme fluxes at the leading edges of a vehicle. Over all the elements that have applications for high temperature environments, There are only three categories of materials of interest for UHTCs: carbides, nitrides and borides [19]. The first is carbides such as HfC and TaC. Materials with carbides as the base compound often have high hardness, high melting temperature and thermally stable properties[20]. These materials are ideal for structural applications under an extreme thermal load such as rocket nozzles [20]; however, they do not have the best oxidation resistance making them an unfriendly option for most other hypersonic applications [19]. The second category of materials is nitrides such as HfN and TaN. These materials are not useful for most hypersonic aerospace applications because despite their great oxidation resistance at high temperatures, they exhibit low oxidation resistance at lower temperatures[20]. There are not many instances in hypersonic aerospace applications where a rapid temperature jump is experienced. For this reason, they will not be discussed further. The last, most promising category of materials is borides such as ZrB<sub>2</sub> and HfB<sub>2</sub>. ZrB<sub>2</sub> was researched for use in propulsion [16]. One draw back of using ceramics in a TPS is their brittle nature. Microscopic effects of such as layers of material in the matrix have yet to be understood [19].

Modeling of ceramic materials used to coat turbine engines as have also been developed. Turbines experience high cyclic temperatures. If these metals were not coated, they would have very short lifespans which increases the cost of sustaining an aircraft. These TPS are often composed of two thin layers, a bond coat (usually an adhesive) and a top coat (a ceramic material like yttria-stabilized zirconia (YSZ)). In order to increase the life cycle, ceramic coatings are applied. These coatings were modeled in the late 1980s through present day in order to understand the

failure behavior using a Finite Element Method (FEM) with temperatures less than  $1200^{\circ}\text{C}$  [21, 22, 23]. Further research was conducted in 2016 by Song et al looked at the formation of the thermally grown oxide layer that forms during the application of the ceramic TBC. This study used an Electron Backscatter Diffraction (EBSD) Scanning Electron Microscope (shown in Fig. 1.2) in to determine the thickness of this third layer of material was  $3.10\ \mu\text{m}$  [24]. More advanced modeling techniques, such as the one presented in this work, need to be developed in order to determine the effect this layer has on the TPS system and its material properties at a macroscopic level.

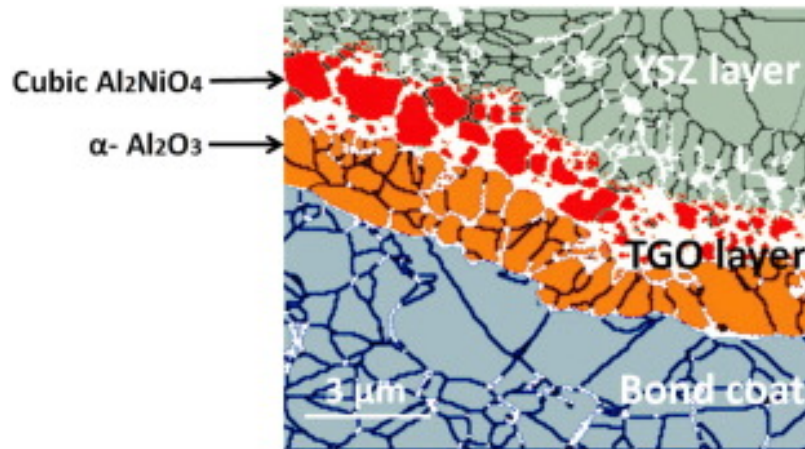


Figure 1.2: EBSD scan of a TBC system showing the layers of materials after the application of YSZ. Reproduced with permission from [24].

There are two common types of composites that could be candidates for advanced TPS; carbon-carbon composites and ceramic matrix composites (CMCs). Both types of TPS use thin layers in order to enhance their existing material properties and extend the period for which these material can perform under hypersonic conditions [19]. The first type is carbon-carbon (c-c) composites. C-C composites are carbon fibers that are set in a carbon matrix [25]. Research has been conducted for decades on how the manufacturing process of carbon fiber effects the resulting preforms material properties [26]. Once the carbon fibers have been manufactured, they are woven

into textile sheets. Then, these sheets are pressed together using a resin or epoxy in order to form a light weight, dense block of material[25]. C-C composites have great material properties such as low density, low coefficient of thermal expansion [16] and thermal shock resistance [25]. All of these properties make c-c composites ideal for hypersonics with one exception; C-C composites oxidize at high temperatures. One method to increase oxidation resistance of c-c composites is to coat the composite with a thin layer of a non-oxidizing material. There has been extensive experimental research conducted into the best coating material and application method. Ceramics, such as SiC and Si<sub>3</sub>N<sub>4</sub>, are often used as external coatings after the carbon matrix is set due to their performance under extreme conditions [25, 27]. These ceramics are good at preventing oxygen from reaching the material underneath due to their low permeability at high temperatures [25] which would increase the exposure time before material failure [19]. However, at intermediate temperatures, 1500-1800°C, the chemical reactions destroy the protective oxide layer which leads to the destruction of the coating material. If oxygen were to penetrate the c-c composite, pressure could be built up underneath the surface of the coating further compromising the protective layer [25]. In more recent years, there has been a surge in using a class of ceramics known as UHTCs. UHTCs are defined as ceramics that have a melting temperature above 3000°C. There has been a particular focus on using borides such as Zr and Hf in order to increase the effectiveness of the Si [28]. There was also research conducted into finding the optimum coating application method [16], coating material composition [27, 29] and even using multiple material layers for protection [30, 31, 32]. For example, Xu et al [28] experimented on c-c composites with two layers of ZrB<sub>2</sub>-based layers applied inside of a wind tunnel facility.

UHTCs are a great material for hypersonic applications with only one major drawback. UHTCs like all ceramics are brittle. This has led researchers down the path of

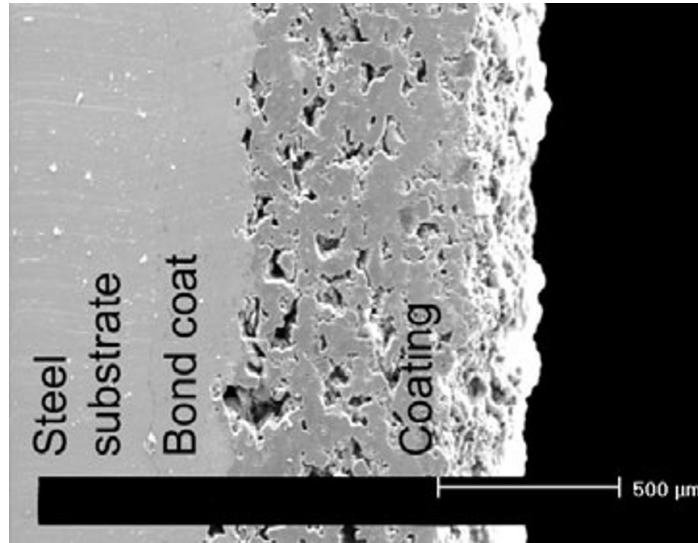


Figure 1.3: SEM images of SiC<sub>3</sub>N<sub>4</sub> coated steel substrate. Reproduced with permission from [27].

looking into ways to reinforce UHTC [33]. Thus, UHTC ceramic matrix composites (CMCs) are the second type composite material of interest for TPS. These composites are ceramics that have been reinforced using ceramic tubes [33]. These tubes, often carbon nano-tubes, help the material by increasing its fracture resistance [34]. While CMCs have been studied for decades, there has been a push in the last decade to study ultra-high temperature ceramic matrix composites (UHTCMCs). Figure 1.4 shows the fabrication process used for making rolled compacted UHTCMCs. These carbon rolls are thin layers of material with different material properties than the surrounding material. Despite the amount of research already conducted into UHTC, Fahrenholtz and Hilmas called for further research to be conducted into using UHTC as advanced TPS in 2017 [19]. They noted the lack of simulations conducted at high temperatures [19] and that simulations are often of the bulk material properties of UHTC and do not account for the carbon that is used to reinforce the ceramic materials [19]. There is still research to be conducted into modeling the non-uniform composition of ceramics used in UHTC[19].

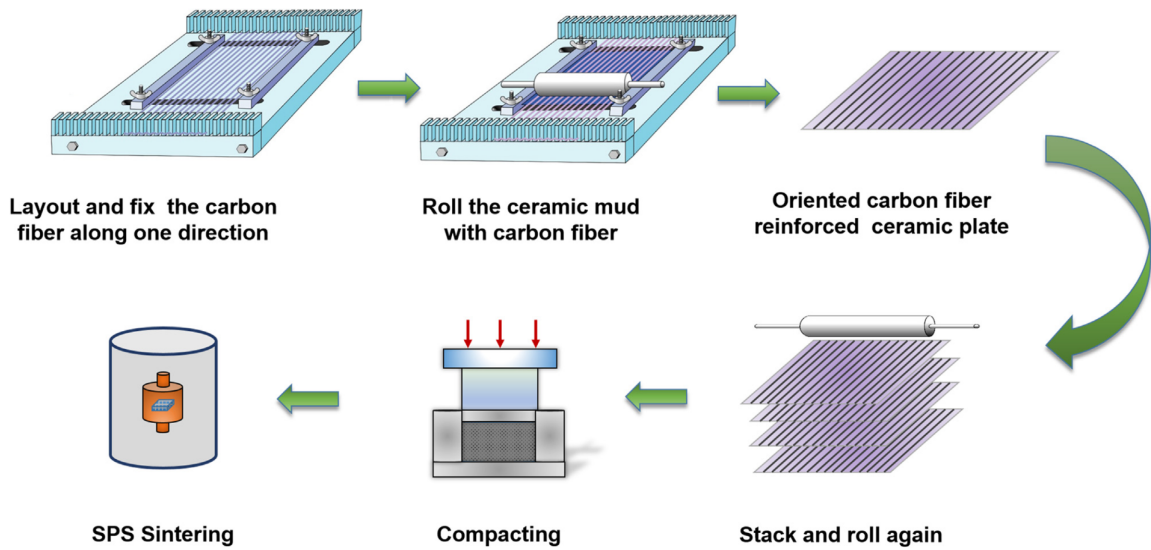


Fig. 1. The schematic diagram of fabrication.

Figure 1.4: Carton of the manufacturing process for rolled compacted UHTCMC fabrication. Reproduced with permission from [34]

The last classification of material is ablative TPS. These materials were first theorized and developed by George Sutton in 1957 [15, 35]. In a 1960 publication, Sutton himself noted that since ablation constantly decreased the volume of the material by removing the surface material through aero-thermodynamic heating, these materials would need to have low thermal conductivity and high delta in enthalpy [36]. These materials are able to absorb the heat and transfer the kinetic energy into chemical reactions and potential energy that the spacecraft encounters when traveling under hypersonic conditions; thus, slowing down the vehicle upon entry an atmosphere. This is accomplished due to the material construction. The most famous ablative materials are Avcoat which was used on the Apollo ear spacecraft [?] and Phenolic-Inpregnated Carbon Ablator (PICA) which was used on the Mars Science Labratory(MSL) and Stardust [37, 38]. Avcoat was fabricated using a honeycomb structure composed of phenolic reinforced with fiberglass. The honeycomb structure was filled using silica-fiber compound[35]. Ablative materials are effective because



the resin and the atmosphere mixed with the extreme heat produce a pyrolysis gas that travels out of the material. This is known as the char phase shown in Fig. 1.5. As the gas leaves the material, it pushes and extends the thermal boundary layer further away from the structural material of the vehicle. This means that the vehicle experiences less heating overall [35].

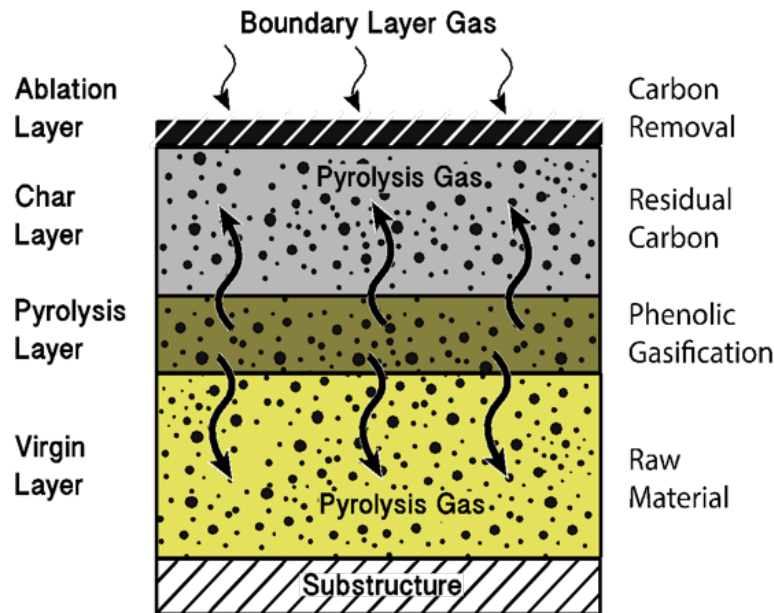


Figure 1.5: Cartoon of the ablation process and the different stages of the material. Reproduced with permission from [39]

Thin layers of material are a part of ablative TPS as well. In order to protect the ablative material from absorbing water, thin layers are applied. MSL has a thin layer of silicone was applied [40]. If water is adsorbed into the material, it need to be kept underneath the protective layer because when the water is heated it expanded and has the potential to spallate. Spallation leads to uneven surfaces which leads nonuniform recession of the material. It was shown in 2016 that the presence of water could have accounted for the abnormality seen in the thermocouple data collected from the MSL heatshield [41]. Ceramic thin layer coatings are also used to protect ablative TPS

from Micro-Meteoroid Orbital Debris (MMOD) collisions during flight in space [42]. If a MMOD would collide with an unprotected TPS, the TPS material would be damaged. This damage would compromise the TPS, which could result in a total failure of the TPS due to nonuniform heating. A thin layer of pore sealer is often applied to protect the TPS prior to launch. The water in the material would vent during the cruise stage, and could damage sensitive part of the vehicle [43]. Finally, large TPS systems are often made of tiles which require a bonding agent to be applied to attach the TPS tiles to the vehicle and to bond the tiles to each other [38]. These thin layers could have a drastic impact on the performance of the TPS if they do not perform as expected. They could modify the pyrolysis flow and heat penetration. This complex physical phenomena is difficult to test on a single experimental ground facility and requires modeling and simulations to be conducted in order to keep testing costs under control. The two factors that drive up testing costs are the costs to run the experimental facilities and the destruction of the materials. Hence, a great effort has been taken to model the complex behavior of ablative materials.

Over the years, several codes have been developed to model ablative TPS. Charring Materials Ablation (CMA) was developed in the 1950s and 1960s by Aerotherm Cooperation [44]. CMA was a one-dimensional finite difference solver that modeled the pyrolysis phenomenon loosely coupled with the energy equation [44]. This code served as the industry standard for several decades. Since this first modeling code, there have been several others developed that have expanded the knowledge and understanding of how ablative materials respond to extreme re-entry conditions. Most recently, codes such as CHAR [45], 3-dimensional Fully Implicit Ablation and Thermal (3dFIAT) response solver [46], LeMANS [47] and Kentucky Aerodynamic Thermodynamic Solver(KATS) [48] have contributed to the field by expanding the solution from one-dimension to three dimension, solving more than just one equation,

understanding the chemical decomposition and how that affects the flow around the capsule. However, one area that all of these state-of-the-art codes neglect when solving the ablation problem is modeling the thin layers of material used in a TPS. Based on these findings, it is clear that there is a need to accurately model the effect of the thin layer in TPS. The research that has been conducted on modeling thin layers was focused on modeling ceramics layers using finite element models. One research group developed a finite element model that simulates the aerodynamic heating that occurs on a hypersonic vehicle while in flight [49]. The model was validated using an ANSYS produced temperature profile of the nose cap where the errors in the data were attributed to uncertainties in the measurements as well as an inconsistency in the consideration of the thermal contact resistance between the coating and surface of the cone [49]. Another group used a phase field model in order to capture oxidation of a multi-phase material such as an UHTC coatings. The SiC material melts while the  $ZrB_2$  does not under the extreme conditions [50]. It was found that the more SiC in the coating, the faster the oxidation rate of the  $ZrB_2$ -SiC [50]. This effect was more pronounced at sharp corners [50].

Copyright© Christen Setters, 2021

<https://orcid.org/0000-0003-2346-3713>

## Chapter 2 Methodology & Verification

### 2.1 Volume-Averaging Flux-Conservation Method

The Kentucky Aerodynamic Thermodynamic System Material Response code (KATS-MR) is a finite-volume solver used to model TPS materials under hypersonic aerothermodynamic heating conditions. It solves the conservation of mass, momentum and energy for compressible gas flow in porous media [48]. The KATS framework has been used to model various hypersonic-related applications [51, 52, 18, 53, 54]. The governing equations take the form of

$$\frac{\partial \mathbf{Q}}{\partial t} + \nabla \cdot (\mathbf{F}_a - \mathbf{F}_d) = \mathbf{S} \quad (2.1)$$

where

$$\mathbf{Q} = \begin{pmatrix} \phi \rho_{g_1} \\ \vdots \\ \phi \rho_{g_{ngs}} \\ \rho_{s_1} \\ \vdots \\ \rho_{s_{nss}} \\ \phi \rho_g u \\ \phi \rho_g v \\ \phi \rho_g w \\ \phi E_g + E_s \end{pmatrix}, \quad \mathbf{P} = \begin{pmatrix} p_1 \\ \vdots \\ \rho_{g_{ngs}} \\ \rho_{s_1} \\ \vdots \\ \rho_{s_{nss}} \\ \phi \rho_g u \\ \phi \rho_g v \\ \phi \rho_g w \\ \phi E_g + E_s \end{pmatrix}, \quad \mathbf{S} = \begin{pmatrix} \omega_{g_1} \\ \vdots \\ \omega_{g_{ngs}} \\ \omega_{s_1} \\ \vdots \\ \omega_{s_{nss}} \\ D_x \\ D_y \\ D_z \\ S_D \end{pmatrix} \quad (2.2)$$

and

$$\mathbf{F}_a = \begin{pmatrix} \phi\rho_{g_1}u & \phi\rho_{g_1}v & \phi\rho_{g_1}w \\ \vdots & \vdots & \vdots \\ \phi\rho_{g_{ngs}}u & \phi\rho_{g_{ngs}}v & \phi\rho_{g_{ngs}}w \\ 0 & 0 & 0 \\ \vdots & \vdots & \vdots \\ 0 & 0 & 0 \\ \phi\rho_g u^2 + p & \phi\rho_g uv & \phi\rho_g uw \\ \phi\rho_g uv & \phi\rho_g v^2 + p & \phi\rho_g vw \\ \phi\rho_g uw & \phi\rho_g vw & \phi\rho_g w^2 + p \\ \phi\rho_g uH & \phi\rho_g uH & \phi\rho_g uH \end{pmatrix}, \mathbf{F}_d = \begin{pmatrix} 0 & \dots & 0 \\ \vdots & \vdots & \vdots \\ \vdots & \vdots & \vdots \\ \vdots & \vdots & \vdots \\ \vdots & \vdots & \vdots \\ 0 & \dots & 0 \\ F_{cond,y} & F_{cond,x} & F_{cond,z} \end{pmatrix}. \quad (2.3)$$

In order to model thin layers of materials, a flux-splitting volume-averaging method is introduced. Figure 2.1 illustrates the approach by depicting the thin layer of material and the bulk material in the same computational domain. The flux on each side

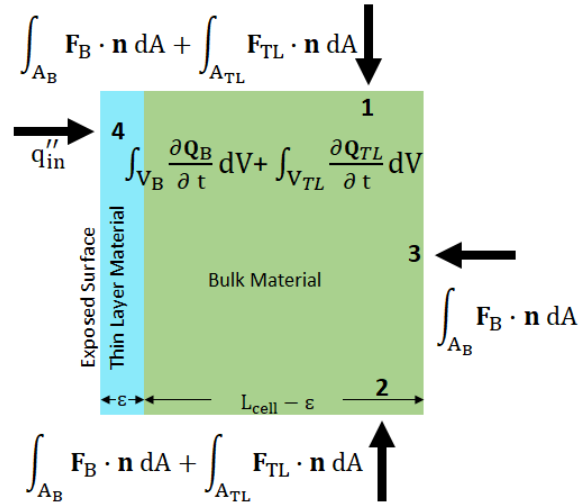


Figure 2.1: Hybrid cell containing bulk (green) and thin layer (light blue) materials. The fluxes on each side of the cell represent the exchange of conserved properties between the neighboring cells.

of the cell represent the exchange of conserved properties between the neighboring cells. The thin layer is assumed to be a thickness of  $\varepsilon$ , which leads to the definition of the thin layer volume fraction,

$$\zeta_V = \frac{\varepsilon_V}{V_{cell}} \quad \text{and} \quad \zeta_A = \frac{\varepsilon_A}{A_{cell}} \quad (2.4)$$

which have values between  $[0,1]$ . Based on the simplified geometry in Fig. 2.1, this equation becomes:

$$\begin{aligned} \int_V \left[ \zeta_V \frac{\partial \mathbf{Q}_{TL}}{\partial t} + (1 - \zeta_V) \frac{\partial \mathbf{Q}_B}{\partial t} \right] dV + \int_{A_1} [\zeta_{A_1} \mathbf{F}_{TL} + (1 - \zeta_{A_1}) \mathbf{F}_B] \cdot \mathbf{n} dA_1 \\ + \int_{A_2} [\zeta_{A_2} \mathbf{F}_{TL} + (1 - \zeta_{A_2}) \mathbf{F}_B] \cdot \mathbf{n} dA_2 + \int_{A_3} \mathbf{F}_B \cdot \mathbf{n} dA_3 + q''_{in} = 0. \end{aligned} \quad (2.5)$$

If the volume fraction of the bulk material and the area fraction  $A$  is known, at each of the faces, then the control volume analysis becomes

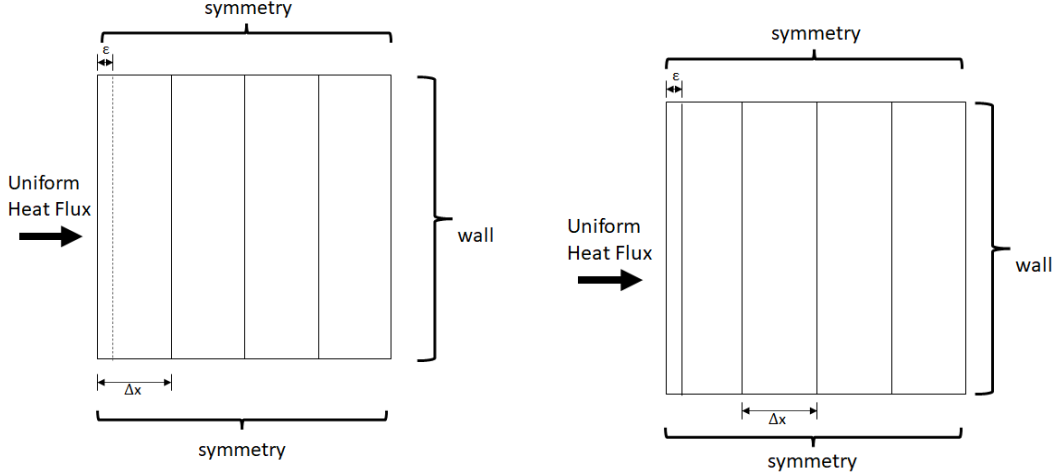
$$\int_{V_B} \frac{\partial \mathbf{Q}_B}{\partial T} dV + \int_{V_{TL}} \frac{\partial \mathbf{Q}_{TL}}{\partial T} dV + \int_{A_B} \mathbf{F}_B \cdot \mathbf{n} dA + \int_{A_{TL}} \mathbf{F}_{TL} \cdot \mathbf{n} dA + q''_{in} = 0 \quad (2.6)$$

For simplicity purposes, it is assumed that no source terms are present, and that the left surface is a boundary condition with an imposed flux of  $q''_{in}$ . This formulation was implemented into KATS MR by defining  $\zeta_V$  at every cell center, and  $\zeta_A$  at every face. If the cell does not contain a thin layer, these parameters were set to 0.

## 2.2 Verification of the Model Using Energy Conservation

This formulation was validated by comparing the state-of-the-art approach - where the thin layer material is resolved over a single cell - with the new volume-average flux-conservation method introduced in this work. A verification test was conducted to insure that the two methods give the same results. The computational domains used to represent the two methods are shown in Figs. 2.2.

The computational domain shown in Fig. 2.2a illustrates the volume-averaging flux-conservation method using  $\zeta$  to represent the thin layer in the first cell. Fig-



(a) Volume-Averaging Flux-Conservation Method

(b) State-of-the-art mesh

Figure 2.2: Computational mesh for a  $25.4 \times 25.4 \text{ mm}^2$  block of material composed of solid metal with a thin layer of material on the surface with thickness  $\varepsilon = 1.5875 \text{ mm}$ .

Figure 2.2b illustrates the state-of-the-art method where the entire thin layer is encapsulated within the first cell. Both blocks are composed of a bulk material with an  $\varepsilon = 1.5875 \text{ mm}$  thin layer applied on the front surface. The block is heated using a uniform heat flux of  $1.0 \times 10^5 \text{ W/m}^2$  applied to the thin layer. The back of the block was treated as an adiabatic wall. The material properties were assumed to be independent of temperature.

To illustrate the method, a simple solid heat conduction case is considered. Assuming that the solid does not decompose, the conservation equation is reduced to the energy equation and simplifies to

$$\frac{\partial E_s}{\partial T} \frac{\partial T}{\partial t} = S_{D_x} + \frac{\partial}{\partial x} q_{cond,x}. \quad (2.7)$$

With conduction taking the form of Fourier's Law and a thermal conductivity independent of temperature, and assuming there are no sources, Eq. 2.7 becomes

$$\rho c_p \frac{\partial T}{\partial t} = \frac{\partial}{\partial x} \left( \kappa \frac{\partial T}{\partial x} \right). \quad (2.8)$$

Applied over the first cell, the finite volume integration developed in Eq. 2.6 yields

$$\rho c_p \int_V \frac{\partial T}{\partial t} dV = \int_A \left[ \zeta_A \kappa_{TL} \left( \frac{\partial T}{\partial x} \right) + (1 - \zeta_A) \kappa_B \left( \frac{\partial T}{\partial x} \right) \right] \cdot \mathbf{n} dA \quad (2.9)$$

It is important to point out that this method preserves the conserved quantities within the cell, and although gradients across the two materials are not resolved, no information is lost.

Each material property  $\rho$ ,  $\kappa$ , and  $c_p$ , were verified in separate cases. First, the densities and specific heat of the thin layer and bulk material are assumed to have the same values while the thermal conductivities of the two materials are assumed to be different. The material properties for both the bulk and thin layer material are shown in Table 2.1.

Table 2.1: Material properties for the  $\kappa$  certification case

$\rho_{TL}$ , kg/m <sup>3</sup>	$c_{p,TL}$ , J/K	$\kappa_{TL}$ , W/m K	$\rho_B$ , kg/m <sup>3</sup>	$c_{p,B}$ , J/K	$\kappa_B$ , W/m K
5000	300	25	5000	300	50

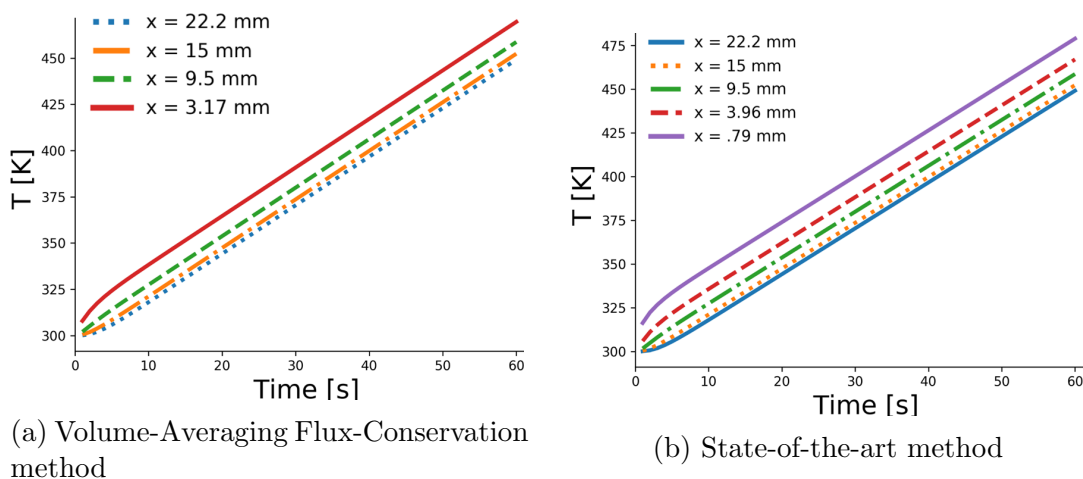


Figure 2.3: Temperatures extracted at cell centers when  $\kappa$  was varied.

In order to compare the two methods, the temperatures were extracted at the cell centers of each domain. The results are plotted in Figs. 2.3. The cell center temperatures of the last three cells from both domains are plotted for comparison in



Figs. 2.4. As can be seen, the results are in excellent agreement. To quantify the difference between the two methods, the  $\|L_2\|$  norm was used

$$\|L_2\| = \sqrt{\frac{\sum_i^3 [u_{B_i} - u_{c_i}]^2}{\sum_i^3 u_{B_i}^2}}. \quad (2.10)$$

and is plotted in Fig. 2.5. The error is small enough to suggest that the two domains produce the same solution.

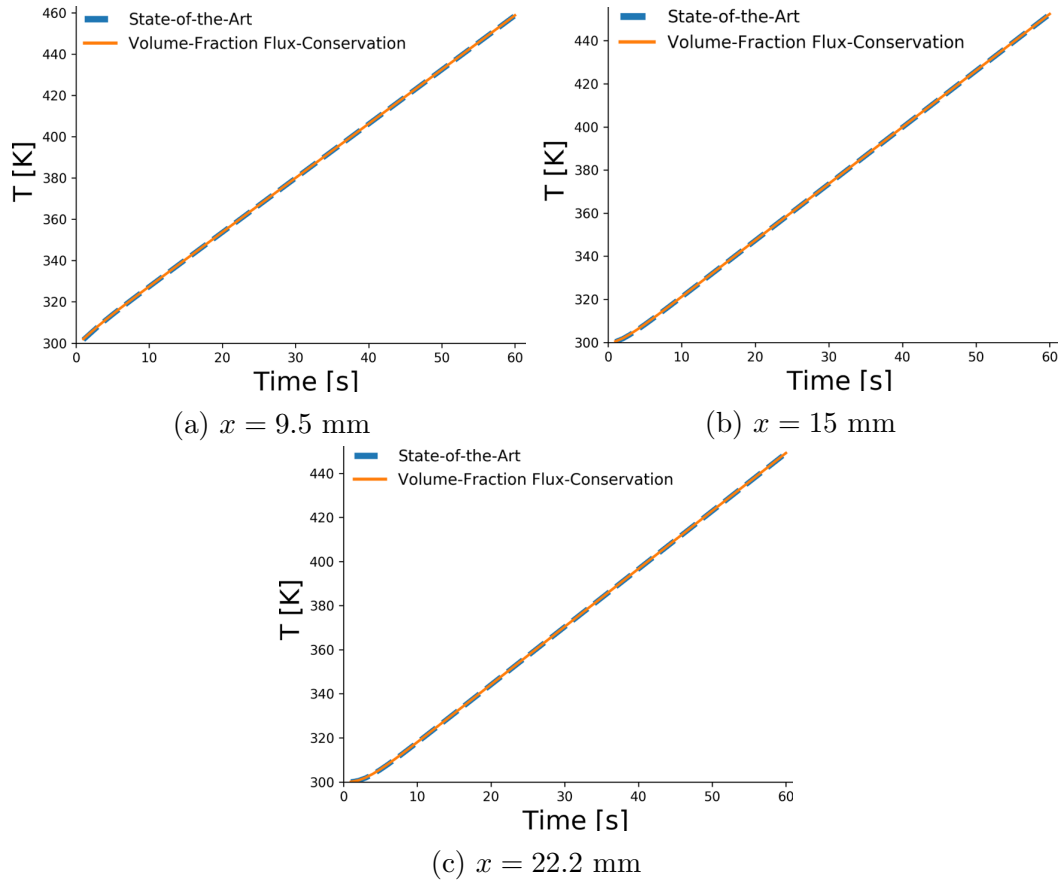


Figure 2.4: Cell center temperatures extracted for both domains when  $\kappa$  was varied.

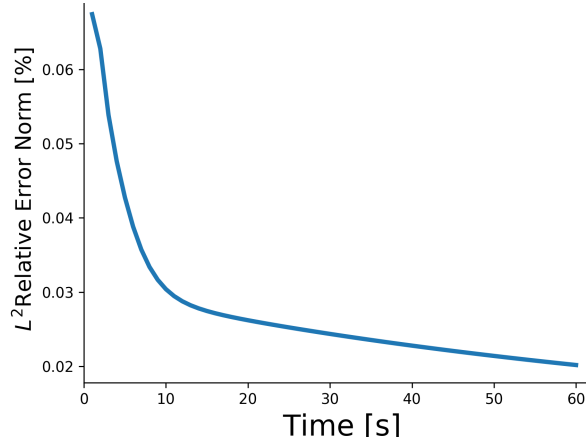
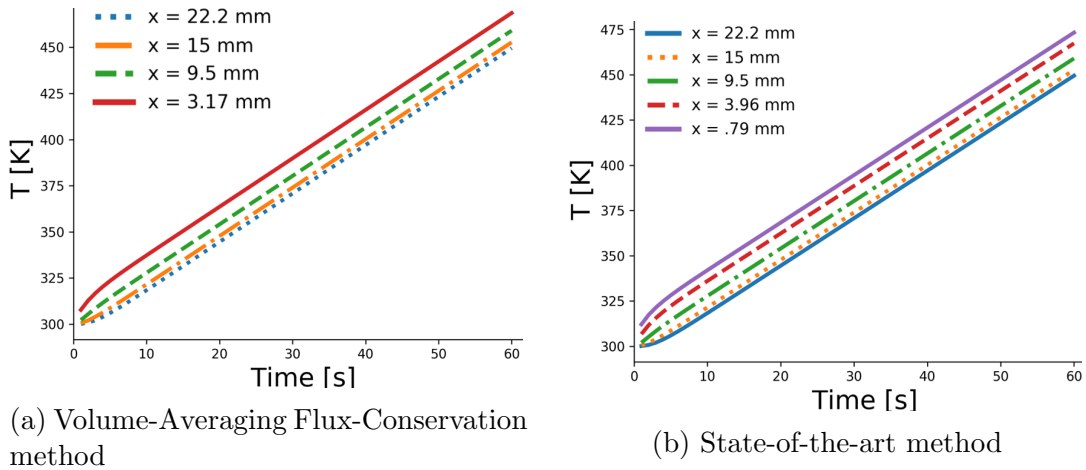


Figure 2.5: The total  $\|L_2\|$  of shared cells as a function of time when  $\kappa$  was varied.

Next, the density and thermal conductivity of the thin layer and bulk material are assumed to have the same values while the heat capacities of the two materials are assumed to be different. The material properties for both the bulk and thin layer material are shown in Table 2.2.

Table 2.2: Material properties for  $c_p$  verification case

$\rho_{TL}$ , kg/m <sup>3</sup>	$c_{p,TL}$ , J/K	$\kappa_{TL}$ , W/m K	$\rho_B$ , kg/m <sup>3</sup>	$c_{p,B}$ , J/K	$\kappa_B$ , W/m K
5000	600	50	5000	300	50



(a) Volume-Averaging Flux-Conservation method

(b) State-of-the-art method

Figure 2.6: Temperatures extracted at cell centers when  $c_p$  was varied.

In order to compare the two methods for this variable, the temperatures were

again extracted at the cell centers of each domain. The results are plotted in Fig. 2.6. The cell center temperatures of the last three cells from both domains are plotted for comparison in Fig. 2.7. As can be seen, the results are in excellent agreement. To quantify the difference between the two methods, the  $\|L_2\|$  norm was used again and was plotted in Fig. 2.8. The error is small enough to suggest that the two domains produce the same solution.

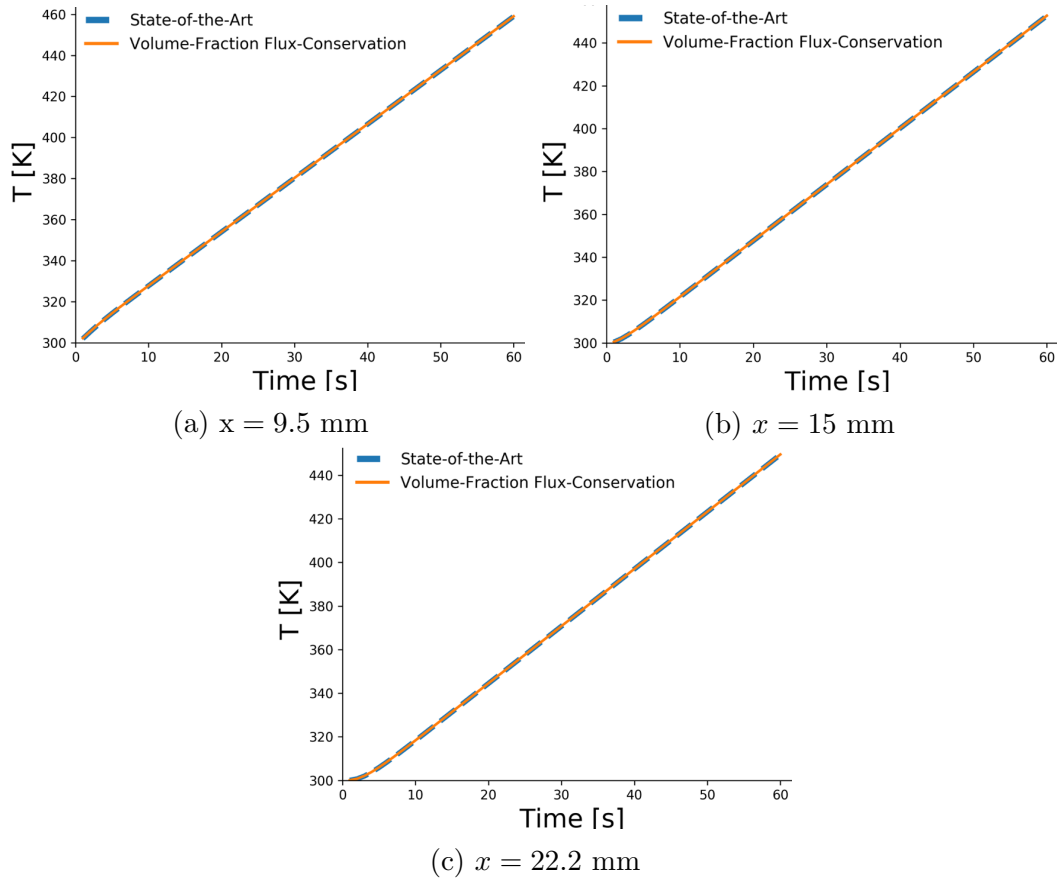


Figure 2.7: Cell center temperatures extracted for both domains when  $c_p$  was varied.

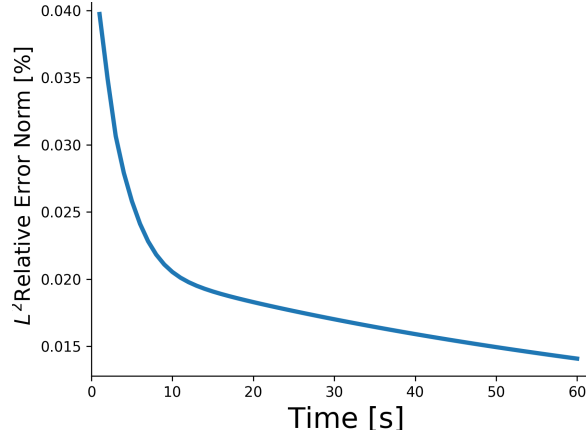


Figure 2.8: The total  $\|L_2\|$  of shared cells as a function of time when  $c_p$  was varied.

Next, the heat capacity and thermal conductivity of the thin layer and bulk material are assumed to have the same values while the densities of the two materials are assumed to be different. The material properties for both the bulk and thin layer material are shown in Table 2.3.

Table 2.3: Material properties for  $\rho$  verification case

$\rho_{TL}$ , kg/m <sup>3</sup>	$c_{p,TL}$ , J/K	$\kappa_{TL}$ , W/m K	$\rho_B$ , kg/m <sup>3</sup>	$c_{p,B}$ , J/K	$\kappa_B$ , W/m K
10000	300	50	5000	300	50

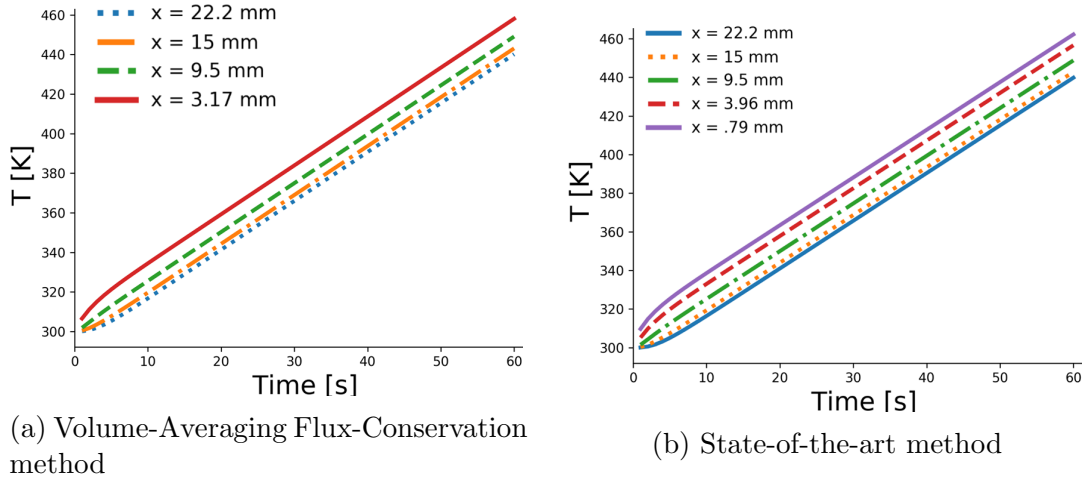


Figure 2.9: Temperatures extracted at cell centers when  $\rho$  was varied.

In order to compare the two methods for this variable, the temperatures were again

extracted at the cell centers of each domain. The results are plotted in Figs. 2.9. The cell center temperatures of the last three cells from both domains are plotted for comparison in Figs. 2.10. As can be seen, the results are in excellent agreement. To quantify the difference between the two methods, the  $\|L_2\|$  norm was used again and was plotted in Fig. 2.14. The error is small enough to suggest that the two domains produce the same solution.

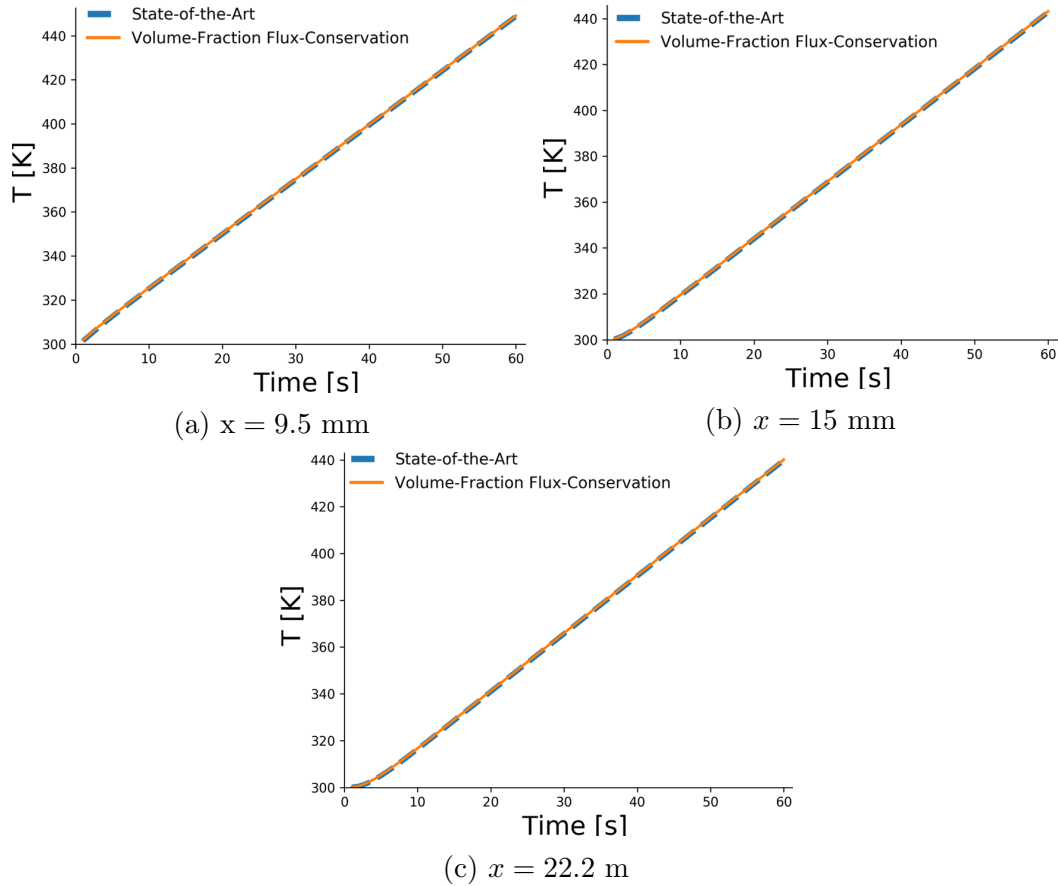


Figure 2.10: Cell center temperatures extracted for both domains when  $\rho$  was varied.

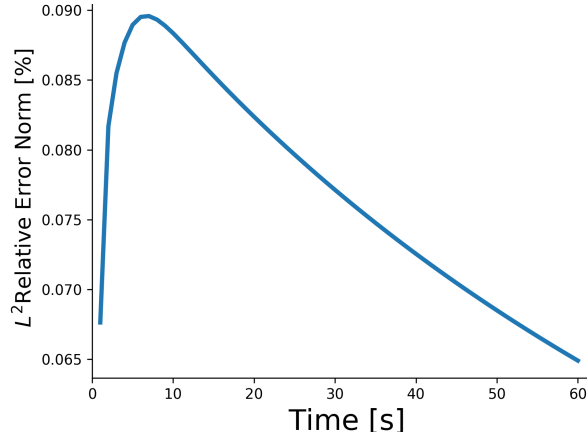


Figure 2.11: The total  $\|L_2\|$  of shared cells as a function of time when  $\rho$  was varied.

Since the error was small for each of the variables, it was concluded that the two methods produce the same solution. It is important to note that the grids used for the above studies were under-resolved. This caused inherent errors in the solutions of both the methods. However, the under resolution of the mesh does not change the outcome of the validation.

The next set of verification cases conducted used the domain for the Volume-Averaging Flux-Conservation method shown in Fig. 2.2a. The first test case was conducted using the material properties shown in Table 2.4 where the first cell had a  $\zeta = 0.25$ . The second test case was conducted using the material properties in Table 2.5 with a  $\zeta = 0.50$  in the first cell. In order to verify that the effective thermal conductivity was the same for both cases in the first cell(s) using the volume-averaging flux-conservation domain. For  $\zeta = 0.25$ ,

$$\kappa_{eff,0.25} = (1 - \zeta)\kappa_B + \zeta\kappa_{TL} = 80 \quad (2.11)$$

Moreover for  $\zeta = 0.50$ ,

$$\kappa_{eff,0.25} = (1 - \zeta)\kappa_B + \zeta\kappa_{TL} = 80 \quad (2.12)$$

The cell center temperatures were extracted and plotted in Fig 2.12. As before, the

Table 2.4: Material Properties for  $\zeta = 0.25$  Verification Case

$\rho_{TL}$ , kg/m <sup>3</sup>	$c_{p,TL}$ , J/K	$\kappa_{TL}$ , W/m K	$\rho_B$ , kg/m <sup>3</sup>	$c_{p,B}$ , J/K	$\kappa_B$ , W/m K
5000	300	20	5000	300	100

Table 2.5: Material Properties for  $\zeta = 0.50$  Verification Case

$\rho_{TL}$ , kg/m <sup>3</sup>	$c_{p,TL}$ , J/K	$\kappa_{TL}$ , W/m K	$\rho_B$ , kg/m <sup>3</sup>	$c_{p,B}$ , J/K	$\kappa_B$ , W/m K
5000	300	60	5000	300	100

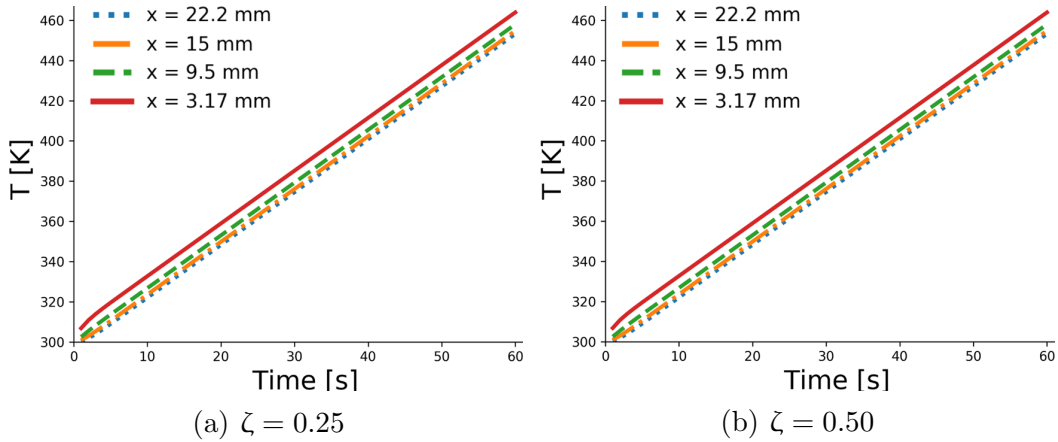


Figure 2.12: Temperatures extracted at cell centers from the volume-averaging flux-conservation domain with the two different thin layers thicknesses and material properties.

temperature was plotted for both cases for each cell center. These results are shown in Fig. 2.13.

In order to compare the solutions are, the relative  $L_2$  error norm was used. For these cases the norm was 0. The two blocks results in the exact same solution. Thus, inducing the same effect thermal conductivity results in the same solution despite the test blocks being composed of different thin layers and materials.

The first set of verification cases compared a state-of-the-art domain with the volume-averaging flux-conservation domain. The conclusion from these results was that the methods produced the same solution for each of the variable when tested separately (meaning only one variable was different between the thin layer and bulk material) and when they were all variable were varied between the thin layer and bulk

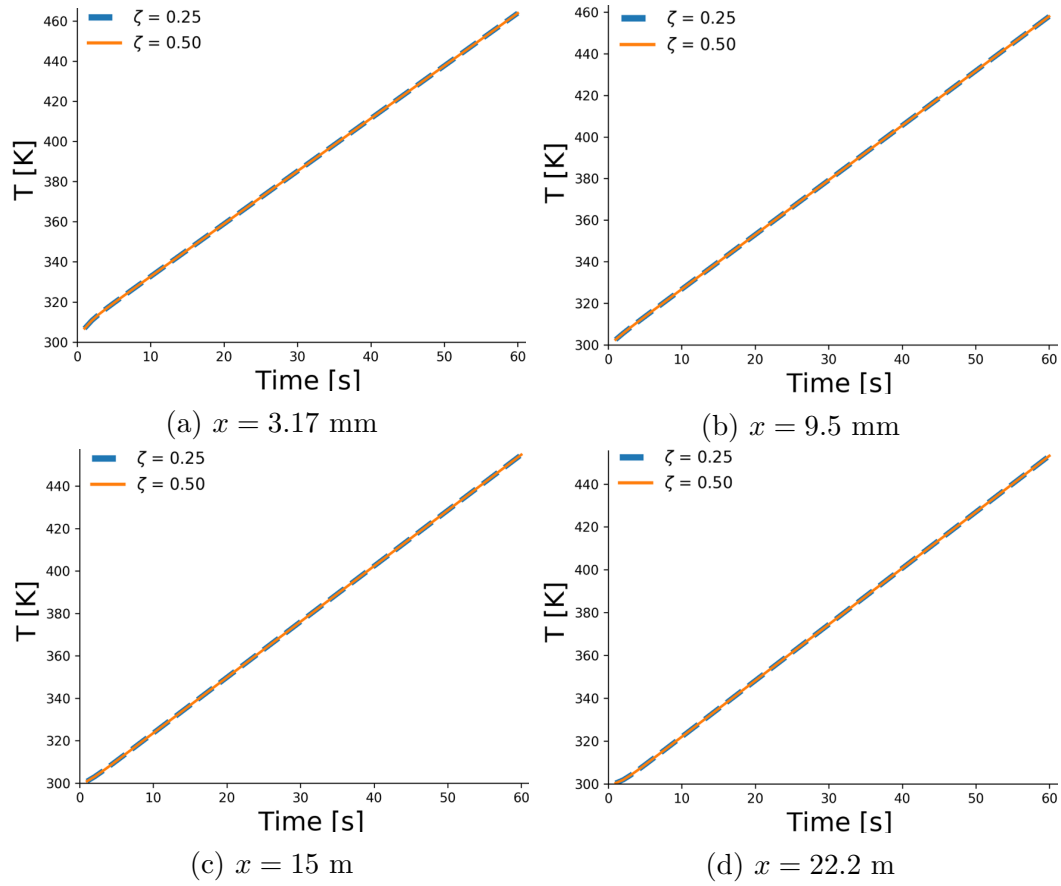


Figure 2.13: Cell center temperatures extracted for both test domains

material. Due to the domains being under-resolved, there were inherent difference in the solutions (leading to the non-zero  $\|L_2\|$ ). Thus, a second set of verification cases was conducted. The goal for the second verification case was to ensure that two blocks with the same effective thermal conductivity produced the same solution.



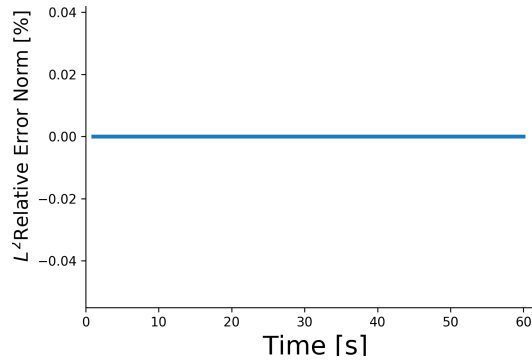


Figure 2.14: The total  $\|L_2\|$  of shared cells as a function of time for  $\zeta = 0.25$  and  $\zeta = 0.50$ .

### 2.3 Verification of Method on Flow through Porous Media

The last verification case conducted on the the Volume-Averaging Flux-Conservation method was to verify that it conserves mass ,energy, and momentum though a porous thin layer by using the pure flow through a porous plug case. Consider the domain Fig. 2.15 where a constant, static pressure gradients applied to both sides of the 0.01 m block of porous material with constant gas and material properties. Flow

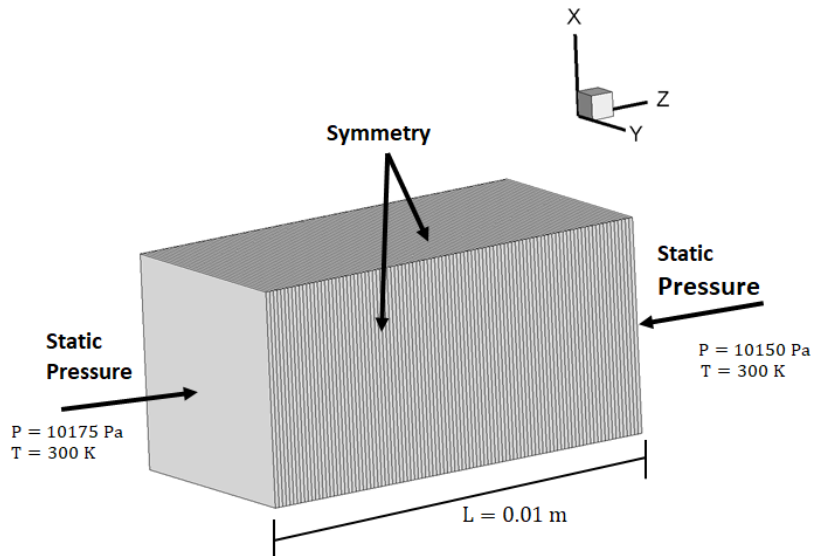


Figure 2.15: One dimensional domain with constant static pressure conditions used as the verification case for the pure flow.

through a porous material is governed by the following equations

$$\frac{\partial(\phi\rho_g)}{\partial t} + \frac{\partial(\phi\rho_g u)}{\partial x} + \frac{\partial(\phi\rho_g v)}{\partial y} + \frac{\partial(\phi\rho_g w)}{\partial z} \quad (2.13)$$

as the conservation of mass,

$$\frac{\partial(\phi\rho_g E_g)}{\partial t} + \frac{\partial(\phi\rho_g u H)}{\partial x} + \frac{\partial(\phi\rho_g v H)}{\partial y} + \frac{\partial(\phi\rho_g w H)}{\partial z} = 0. \quad (2.14)$$

as the conservation of energy and

$$\frac{\partial\rho_g u}{\partial t} + \frac{\partial p}{\partial x} = -\frac{\mu\phi}{K}u \quad (2.15)$$

$$\frac{\partial\rho_g v}{\partial t} + \frac{\partial p}{\partial y} = -\frac{\mu\phi}{K}v \quad (2.16)$$

$$\frac{\partial\rho_g w}{\partial t} + \frac{\partial p}{\partial z} = -\frac{\mu\phi}{K}w. \quad (2.17)$$

with boundary conditions  $T = 300$  K,  $p_{x=0} = 101750$  Pa,  $p_{x=L} = 101050$  Pa,  $u = v = 0$ ,  $\frac{\partial w}{\partial z} = 0$ . The initial conditions at  $t = 0$  s are  $T_0 = 300$  K,  $p_0 = 101050$  Pa and  $u = v = w = 0$ . This case has been previously used to test steady state porous flow, as shown in Weng [48]. Applying a thin layer of material to the block through the Volume-Average Flux-Conservation method leads Eq. 2.17 to become,

$$\frac{\partial\rho_g u}{\partial t} + \frac{\partial p}{\partial x} = -\frac{\mu\phi_{avg}}{K_{avg}}u \quad (2.18)$$

where  $\phi_{avg} = \zeta\phi_{TL} + (1 - \zeta)\phi_B$  and  $K_{avg} = \zeta K_{TL} + (1 - \zeta)K_B$ .

The flow and the material are nonreactive, meaning there are no chemical reactions between the flow and the material. The porous material was assumed to have the material properties of TACOT [48]. The thin layer located at  $\epsilon = 2.5$  mm, measured from the front surface. In the first sample, the thin layer only differed from TACOT by the porosity  $\phi$ , with properties shown in Table 2.6. Since Weng [48] used Darcy's Law to verify that solution was steady state, the thin layer cases were also analyzed using the same approach. At steady state, in one-dimension, Eq. 2.17

$$\frac{\partial(\phi\rho u)}{\partial x} = 0$$

Table 2.6: Porosity: Material properties for block in porous flow verification

$\rho_{TL}$ , kg/m <sup>3</sup>	$c_{p,TL}$ , J/K	$\kappa_{TL}$ , W/m K	$\phi_{TL}$	$K_{TL}$ , m <sup>2</sup>
280	$4.025 \times 10^{-1}$	$9.839 \times 10^{-2}$	$1 \times 10^{-4}$	$1.6 \times 10^{-11}$

which leads to

$$\phi \rho u \equiv \text{const.}$$

This calculation was conducted on the results for the  $\phi$  case and are shown in Fig. 2.16.

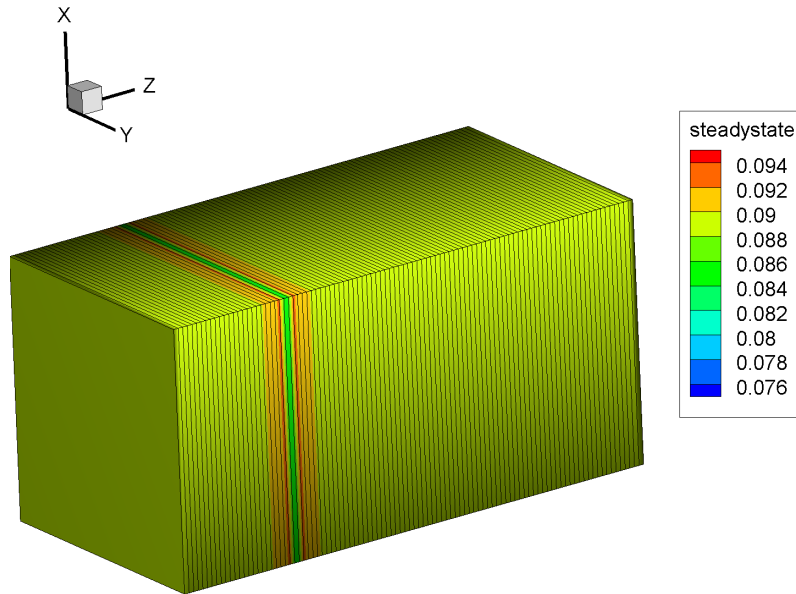


Figure 2.16: Shows the solution is steady state expect for the near the thin layer.

The analysis shows that the solution is not steady state due to the presence of the thin layer. Mass is not being conserved in this case as would be expected. Figure 2.17a shows that the pressure drop across the sample is the same with a thin layer present as it is in the baseline case when there is not a thin layer present. The temperature profile in Fig. 2.17b through the center-line of the material shows an overall decrease in temperature of 7 K from the inlet and outlet temperatures. This change in temperature is centralized at the thin layer and is not seen in the baseline

case. The velocity profile shows the localized instability at the location of the thin layer of material in Fig. 2.17c.

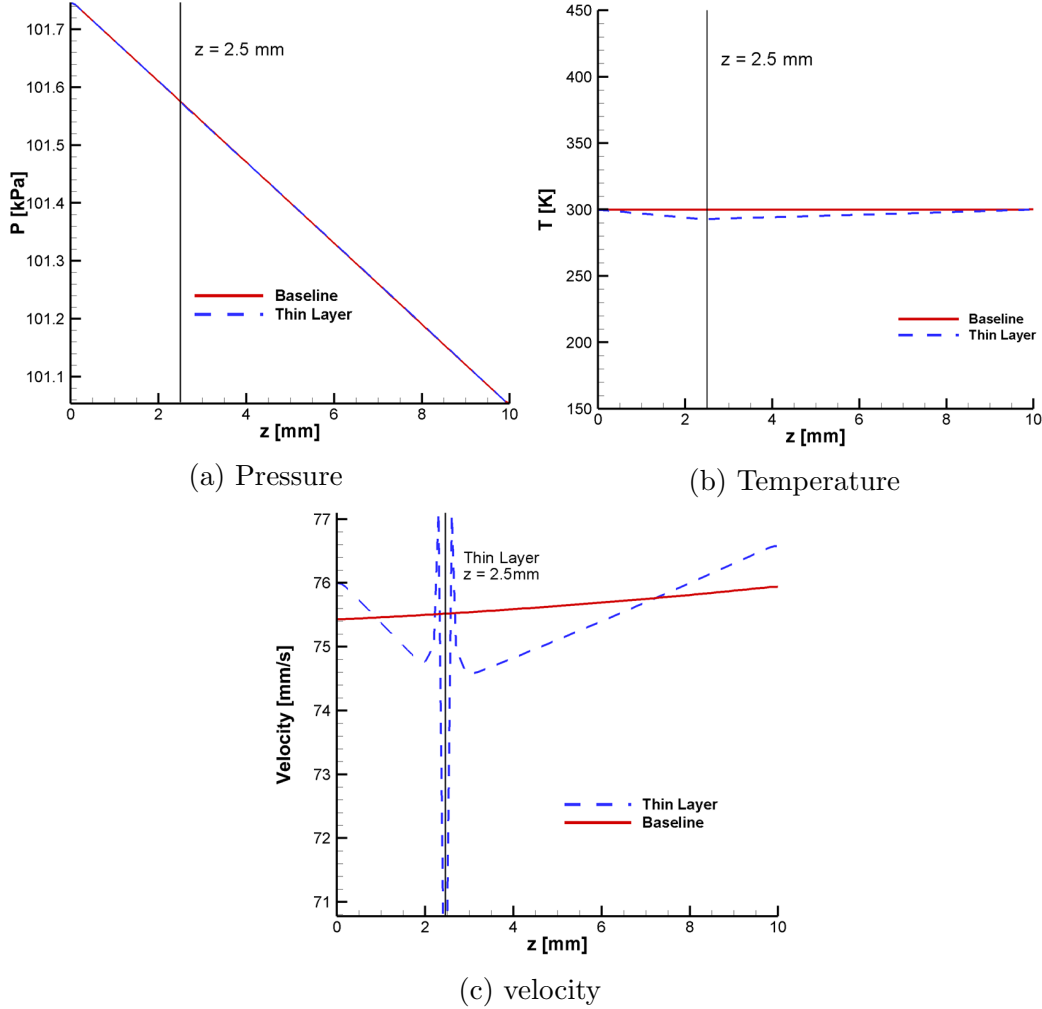


Figure 2.17: Results in (a) show parity between the thin layer and baseline pure flow case when comparing pressure. Temperature profiles in (b) show different profiles but the same gradient across the sample. The velocity profiles (c) show the same general trend in behavior.

As the gas approaches the thin layer, there is a decrease in the velocity profile. After the gas has passed the thin layer, there is a decrease on the other side before the velocity increases before exiting the material. This decrease in velocity is caused by an error in the advective flux scheme that was used. This is shown in the behavior

both temperature and velocity in Fig. 2.17b and Fig. 2.17c. The suspected cause of this discontinuity is attributed to an error in the convective flux schema. As noted by Zhang [53], the AUSM<sup>+</sup><sub>-</sub> up scheme used in this work is known to treat large pressure and velocity changes as a shock. This means that due to the large gradient in velocity at the thin layer the advective flux is treating the thin layer as a shock instead of a wall. This is not the expected behavior and not part of the method itself.

The second sample had only the permeability  $K$  different from the bulk material, with properties shown in Table 2.7.

Table 2.7: Permeability: Material Properties for block in Porous Flow Verification

$\rho_{TL}$ , kg/m <sup>3</sup>	$c_{p,TL}$ , J/K	$\kappa_{TL}$ , W/m K	$\phi_{TL}$	$K_{TL}$ , m <sup>2</sup>
280	$4.025 \times 10^{-1}$	$9.839 \times 10^{-2}$	0.8	$1 \times 10^{-26}$

The behavior was the same when the permeability was the only variable that changed which is shown in Fig. 2.18. As was seen in the porosity case above, the pressure profiles match when permeability was the only variable changed. It should be noted that the permeability for the thin layer is orders of magnitude smaller than the previous case. This difference in magnitude did not create an instability in the solver.

The last thin layer of material changed both the porosity and permeability with properties shown in Table 2.8. Once again, the permeability was approximately zero which did not cause an instability in the solver which was noted to happen in previous work by Weng [48].

Table 2.8: Porosity & Permeability: Material Properties for block in Porous Flow Verification

$\rho_{TL}$ , kg/m <sup>3</sup>	$c_{p,TL}$ , J/K	$\kappa_{TL}$ , W/m K	$\phi_{TL}$	$K_{TL}$ , m <sup>2</sup>
280	$4.025 \times 10^{-1}$	$9.839 \times 10^{-2}$	$1 \times 10^{-4}$	$1 \times 10^{-26}$

The behavior was the same as the previous two cases. The results are shown in

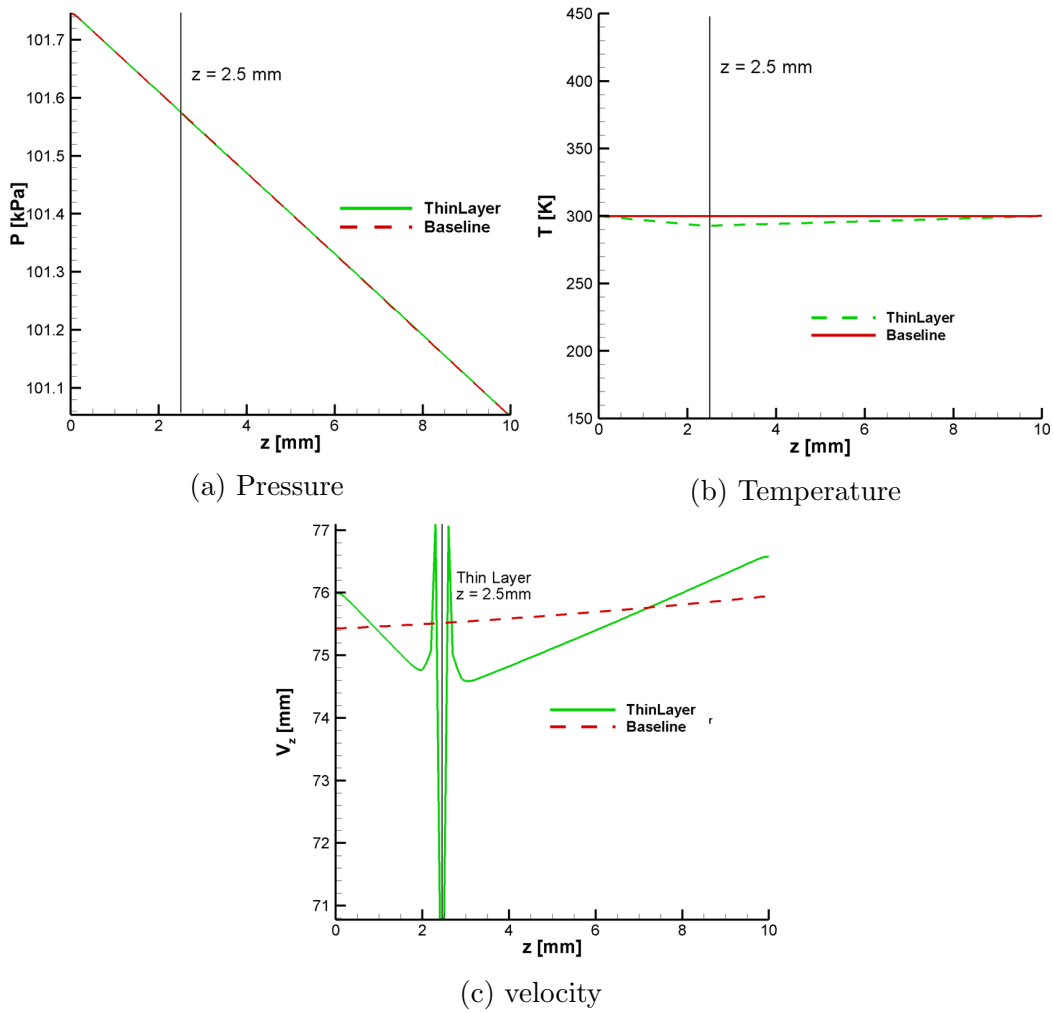


Figure 2.18: Results in (a) show parity between the thin layer and baseline pure flow case when comparing pressure. Temperature profiles in (b) show different profiles but the same gradient across the sample. The velocity profiles (c) show the same general trend in behavior.

Fig. 2.19. As before, the pressures match. The temperature and velocity change as expected in order to conserve energy.

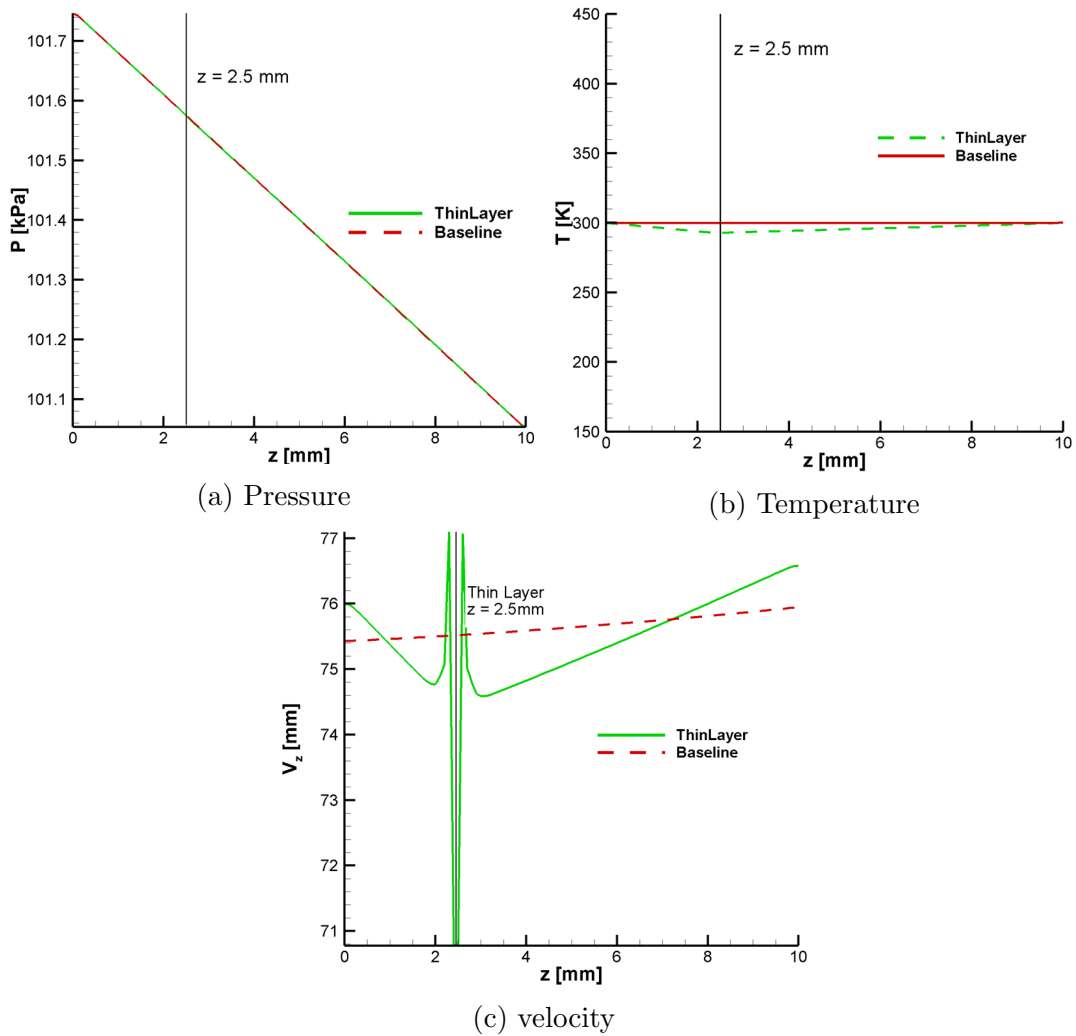


Figure 2.19: Results in (a) show parity between the thin layer and baseline pure flow case when comparing pressure. Temperature profiles in (b) show different profiles but the same gradient across the sample. The velocity profiles (c) show the same general trend in behavior.

The results show that the method works for both the pure heat conduction as well as pure flow. The next sections dives deeper into the method by testing it for full heat conduction in one and two dimensions as well as ablation in one and two dimensions.

Copyright© Christen Setters, 2021

<https://orcid.org/0000-0003-2346-3713>

## Chapter 3 Heat Conduction

### 3.1 One Dimensional Heat Conduction

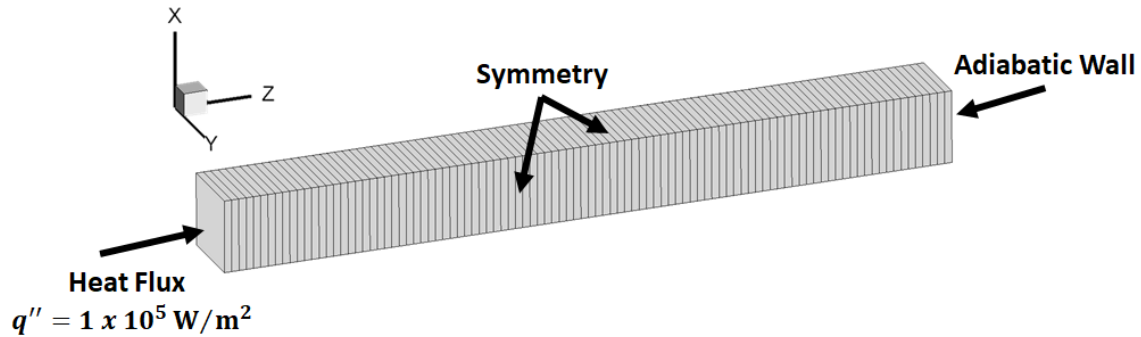


Figure 3.1: Computational domain used for the 1D heat conduction case. The 25 mm bar was composed of 500 cells with uniform spacing.

The effect of a thin layer on the heat profile and the surface temperature of a 1D bar was investigated. The test case consisted of a one-dimensional 25 mm bar with an initial temperature of  $T = 300$  K. The bar is heated using a uniform heat flux of  $1.0 \times 10^5$  W/m<sup>2</sup> on one face, and an adiabatic wall on the opposite face. The other faces were set to symmetry boundary conditions.

A thin layer with thickness  $\epsilon = 0.02$  mm and thermal conductivity  $\kappa = 0.605$  W/m K was applied at the locations shown in the first column of Table 3.1 A baseline case without a thin layer present was also calculated. The location of the thin layer affects how that energy is distributed throughout the bar. As can be seen from Fig. 3.2a, the energy accumulates to the left of the thin layer. The closer the thin layer is to the surface, the less energy in the system has less space to occupy which causes an increase in the temperature at the surface and a drastic decrease in temperature across the thin layer. From Fig. 3.2b, which shows the wall temperatures for each thin layer



location, there seems to be pairing among the solutions for thin layer locations due to the adiabatic boundary condition which imposes a slope matching condition at the back face. For instance, the thin layer at  $z = 6.25$  mm experiences a 4 K increase in surface temperature and has a different profile throughout the material whereas the thin layer at  $z = 12.5$  mm only experiences an increase of 1 K at the same instance in time. It should be noted that the method introduced in this work was not tested for the case of stopping the heat from propagation into the material. Such a case would require a change to the method in order to account for anisotropic material properties.

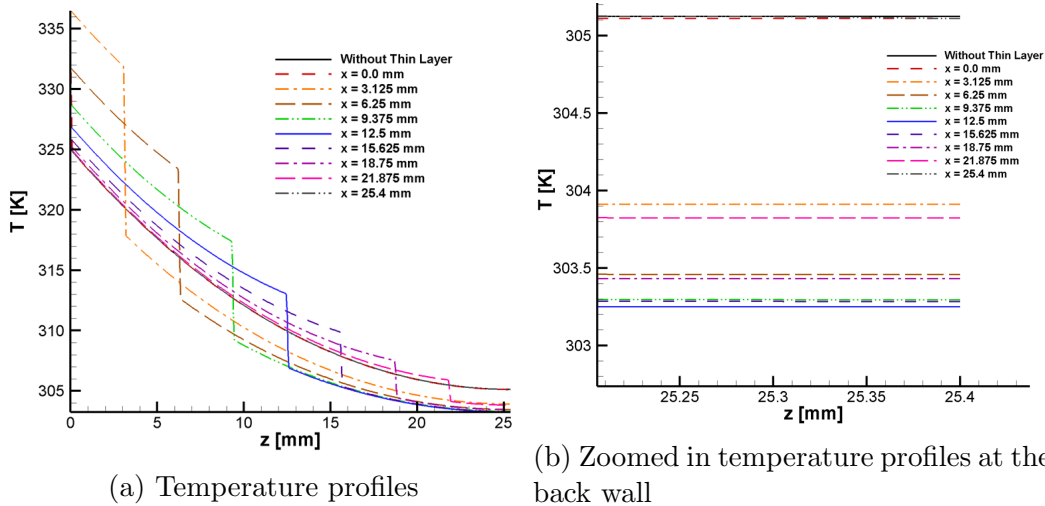


Figure 3.2: Temperature profiles extracted along the  $z$  axis for the 1D heat conduction case for various thin layer locations.

### 3.2 Two-Dimensional Heat Conduction

Next, the multi-dimensional effects of the thin layer are studied using a two-dimensional plate. The computational domain, shown in Fig. 3.3, is a  $20 \times 10$  mm flat plate partitioned into  $80 \times 40$  cells. The material properties were the same as the previous test case (thin layer had a  $\kappa = 6.05$  W/m K). A heat flux of  $1 \times 10^5$  W/m<sup>2</sup> was applied to the front surface. The difference between the wall temperature for each of

Table 3.1: Temperature difference between the case without a thin layer and cases with a thin layer

Location [mm]	T [K]	$\Delta T$ [K]
Without Thin Layer	305.123	0.000
$z = 0.0$	305.109	0.014
$z = 3.125$	303.910	1.213
$z = 6.25$	303.458	1.665
$z = 9.375$	303.294	1.829
$z = 12.5$	303.249	1.874
$z = 15.625$	303.283	1.840
$z = 18.75$	303.430	1.693
$z = 21.875$	303.823	1.300
$z = 25.4$	305.109	0.014

the thin layer locations compared to the baseline case is shown in Table 3.1. The largest difference was found when the thin layer was located at  $x = 12.5$  mm. Thin layers located before the center and after the center move closer to the baseline temperature. A wall prescribed surface temperature of  $T = 300$  K was applied to the opposite face from the applied heat flux. The rest of the faces were assumed to have a symmetry boundary condition.

Figure 3.4a shows the two-dimensional flat plate results without a thin layer. The maximum temperature in the material located at the surface is 333 K. Figure 3.4b shows temperature contours with a thin layer located at  $x = 5$  mm with a uniform thickness  $\varepsilon = 0.025$  mm. The material with the thin layer experienced a maximum temperature of 366 K at the surface. Similarly to the one-dimensional case, the heat is not allowed to flow easily through the material due to the presence of the thin layer, thus increasing the temperature near the surface.

Because of the symmetry, the two-dimensional results of Fig. 3.4 are essentially identically to the one-dimensional case, However, thin layers are not always applied with a uniformly thickness. With the present model, the effects of a non-uniform thin layer thickness can be investigated. In order to represent a non-uniform thickness,

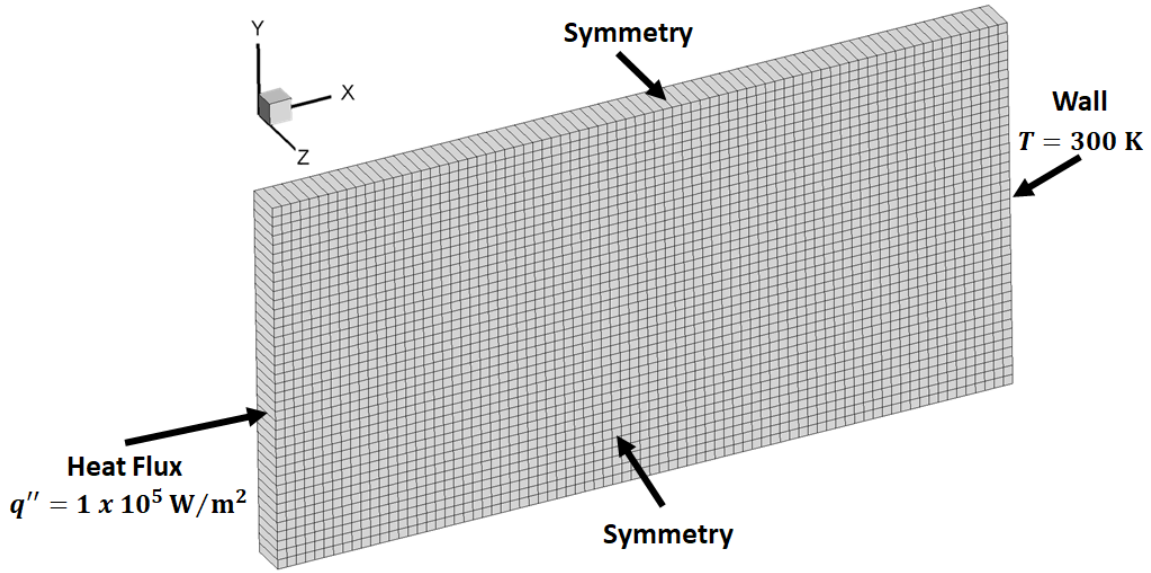


Figure 3.3: Computational domain for 2D heat conduction cases. The  $20 \times 10$  mm flat plate was composed of  $80 \times 40$  cells with uniform spacing.

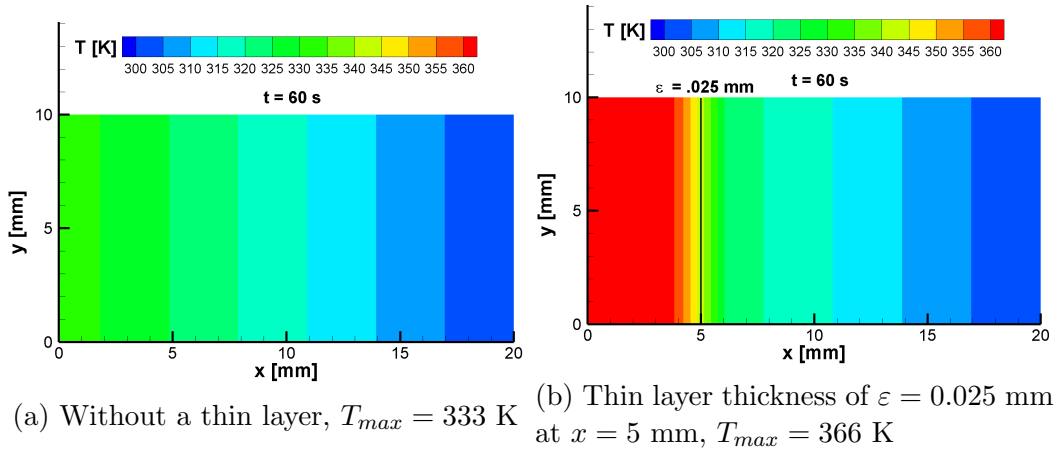


Figure 3.4: Temperature contour for the 2D flat plate

the thin layer thickness was applied using the prescription of the normal distribution below

$$f(x) = \frac{1}{\sigma\sqrt{2\pi}} e^{-\frac{1}{2}\left(\frac{x-\mu}{\sigma}\right)^2} \quad (3.1)$$

where  $\mu$  is a constant. This distribution was chosen since the shape could be tuned using the center position  $\mu$ , which was set at the center of the domain, and the

standard deviation,  $\sigma$ . Three different standard deviations were chosen for this study:  $\sigma = 0.1$  mm which generates a dramatic variation in the thin layer thickness,  $\sigma = 0.25$  mm which was a less dramatic variation and  $\sigma = 0.5$  mm which was a small variation in thin layer thickness. These distributions are shown in Fig. 3.5.

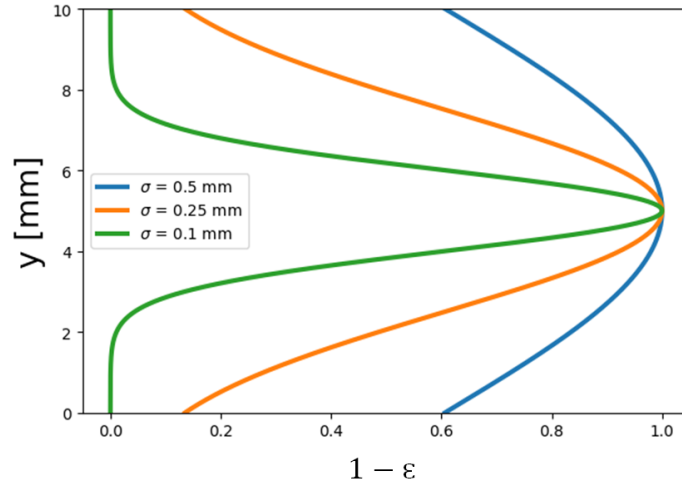


Figure 3.5: The Gaussian distributions for the thin layer thickness,  $\varepsilon$ , for the three different values of standard deviations.

The distribution with a standard deviation of  $\sigma = 0.1$  mm prevented the heat from uniformly penetrating into the material and the resulting temperature distribution shown in Fig. 3.6a. There are regions near the top and bottom of the thin layer where the temperature at the corners, reached a temperature as high as 351 K. This is an increase of  $\approx 20$  K from the results without a thin layer shown in Fig. 3.4a. The heat traveled into the middle of the material where the thin layer was the thinnest which caused the pockets of cooler material to remain at the edges. The distribution with a standard deviation of  $\sigma = 0.25$  mm, shown in Fig. 3.6b, experiences a maximum surface temperature at the corners of 336 K. As expected, the distribution with the largest standard deviation of  $\sigma = 0.5$  mm, shown in Fig. 3.6c, experienced a maximum temperature at the corners with  $T_{max} = 334$  K.

In reality, the thickness of the thin layer is more likely to be random. Therefore, a random  $\varepsilon = [0, 0.25]$  was applied to each cell that contained the thin layer. Thus, the

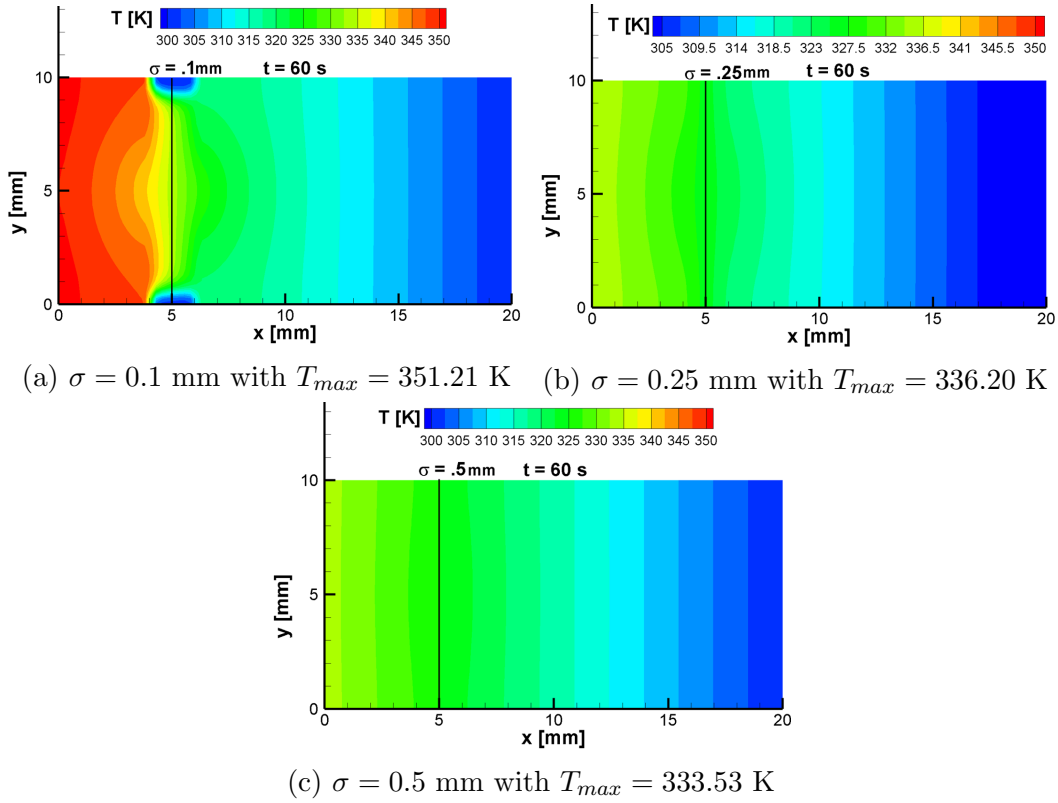


Figure 3.6: Temperature contours for the 2D flat plate with a thin layer present at  $x = 0.5 \text{ mm}$  with Gaussian distribution for  $\varepsilon$

average thickness was  $0.125 \text{ mm}$ . The results for this simulation case are shown in Fig. 3.7. The maximum temperature was found to be  $T = 338 \text{ K}$  at the surface. This is still an increase of  $\approx 5 \text{ K}$ . The result is similar to the results shown in Fig. 3.4a.

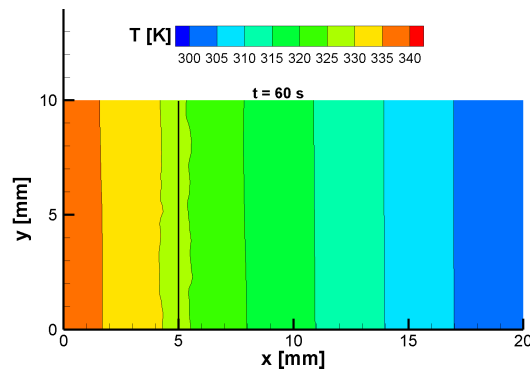


Figure 3.7: 2D flat plate with a thin layer  $x = 0.5 \text{ mm}$  where  $\varepsilon$  was randomly assigned a value such that  $0 \leq \varepsilon \leq .25 \text{ mm}$  where the average was  $\varepsilon = 0.125 \text{ mm}$ .

Copyright© Christen Setters, 2021  
<https://orcid.org/0000-0003-2346-3713>

## Chapter 4 Material Response of Porous Charring Ablator

### 4.1 One Dimensional Charring Ablator

The thin layer volume and area fraction methodology was implemented into rest the governing equations of the material response solver, Kentucky Aerodynamic Thermodynamic Solver-Material Response (KATS-MR). In order to affect the gas transport, the flux modification approach was applied to the advective flux containing permeability  $K$  and porosity  $\phi$ . The TACOT [48] material model was used to represent an ablative material while the thin layer material properties are based on properties of a ceramic material, shown in Table 4.1.

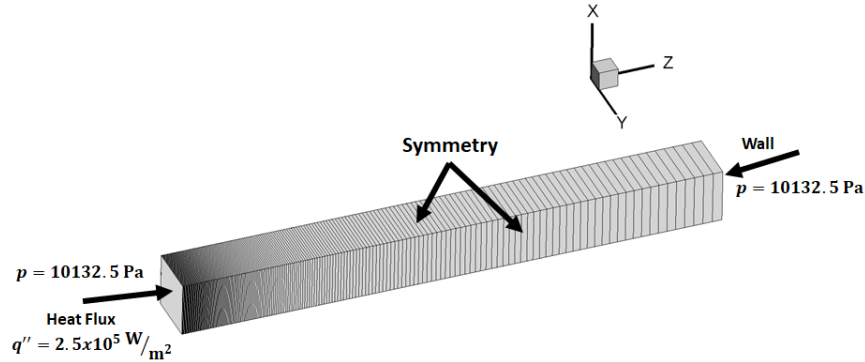


Figure 4.1: Computational domain used for the 1D porous media case. The 100 mm bar was composed of 200 cells with non-uniform spacing

Table 4.1: Material Properties for thin layer for the Porous Flow Verification

$\rho_{TL}$ , kg/m <sup>3</sup>	$c_{p,TL}$ , J/K	$\kappa_{TL}$ , W/m K	$\phi_{TL}$	$K_{TL}$ , m <sup>2</sup>
3210	750	20.7	0.001	$1 \times 10^{-13}$

The initial conditions for the material were  $T = 300$  K and  $p = 10132.5$  Pa. The boundary conditions were set as shown in Fig. 4.1. The computational domain

consisted of 200 cells with non-uniform spacing. A prescribed pressure boundary condition of  $p = 10132.5 \text{ Pa}$  was applied to the wall and the face that was being heat with a flux of  $2.5 \times 10^5 \text{ W/m}^2$ . The results for the case without a thin layer are shown in Fig 4.2.

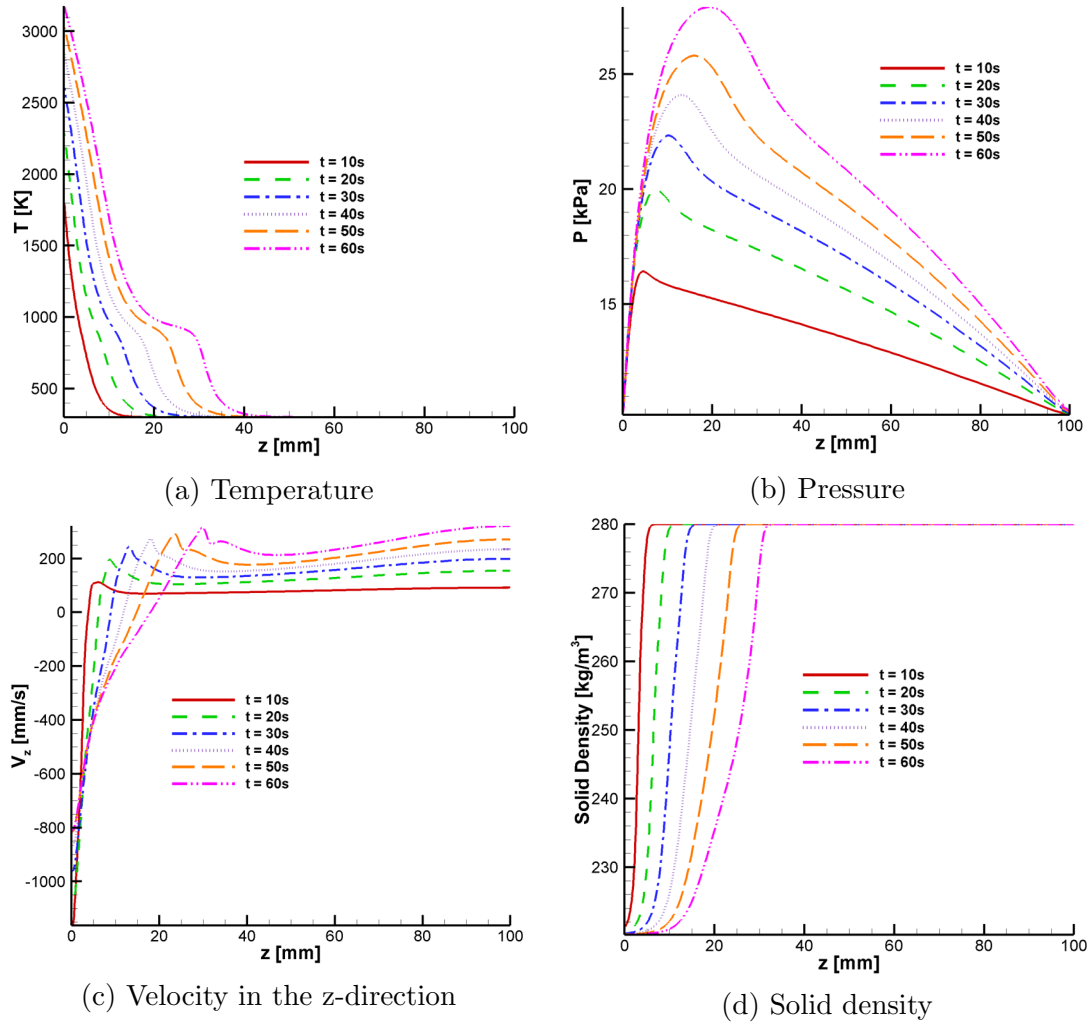


Figure 4.2: Solution profiles for a 1D bar of TACOT material without a thin layer.

These results are what is expected for a one-dimensional charring ablator. The temperature increases on the front surface over time while the ablation of the material change the temperature profile, shown in Fig. 4.2a. The pressure in the material increase as the material ablated over time. Fig. 4.2b also shows that as the ablation



front moves through the material, the peak pressure follows. The velocity profiles extracted at the centerline also follow the ablation front. The peak velocity corresponds to the location of the ablation front which can be seen in Fig. 4.2c. The solid density plotted in Fig. 4.2d shows that the material is, in fact, ablating.

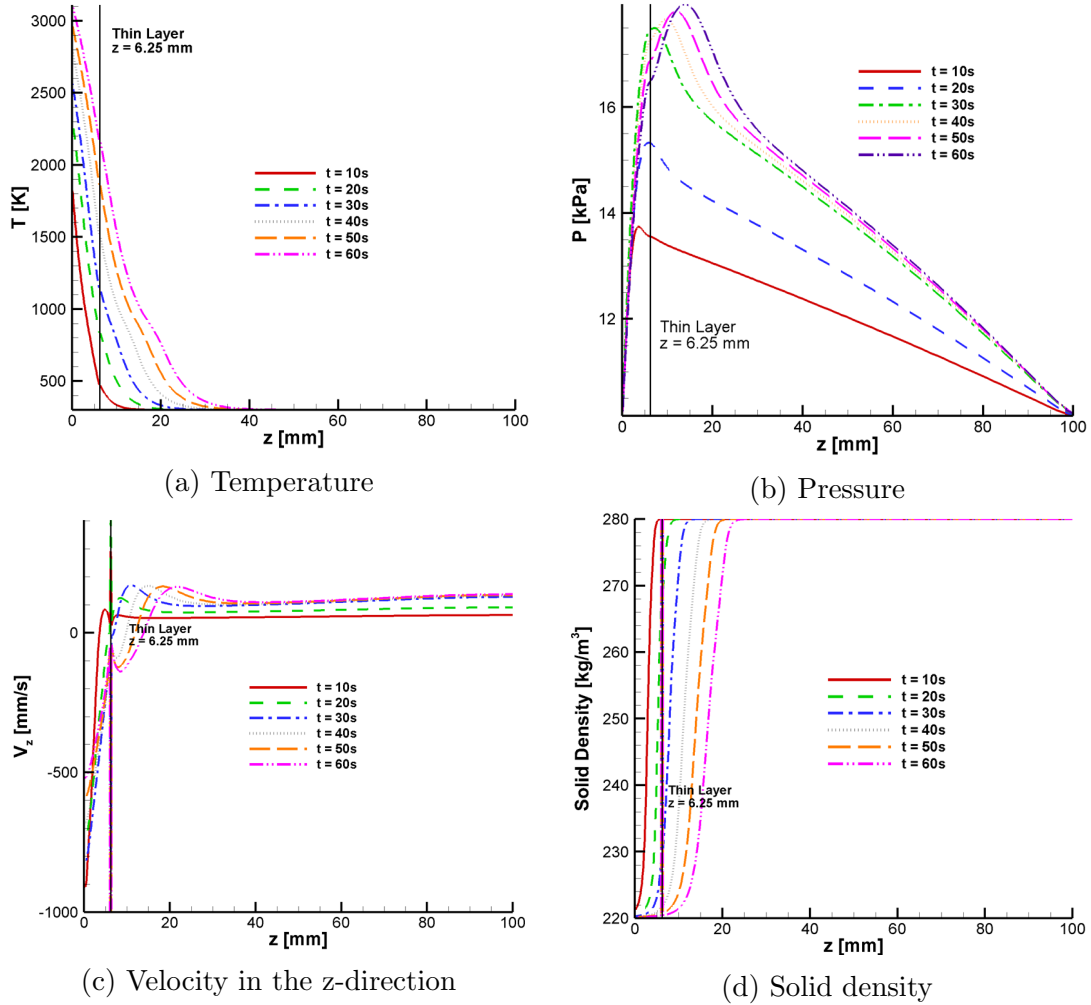


Figure 4.3: Solution profiles for a 1D bar of TACOT material with a thin layer at  $z = 6.25$  mm.

The same conditions were used to run the case with thin layer at  $z = 6.25$  mm with thickness  $1.5 \times 10^{-1}$  mm. These results are shown in Fig. 4.3. In order to better understand the effect the thin layer had on ablation the results for each variable were plotted at  $t = 60$  s for the case without a thin layer and with a thin layer. First,

the temperature profiles show different behavior when the thin layer is present versus when it is not. The presence of the thin layer flattens the temperature bump that is due to the decomposition of the material between the virgin and char material properties. As can be seen in Fig. 4.4, there is still a slight bump when the thin layer is present but it is far less pronounced than in the traditional ablation case. The thin layer also sees a slight decrease in surface temperature when compared to the TACOT bar without a thin layer.

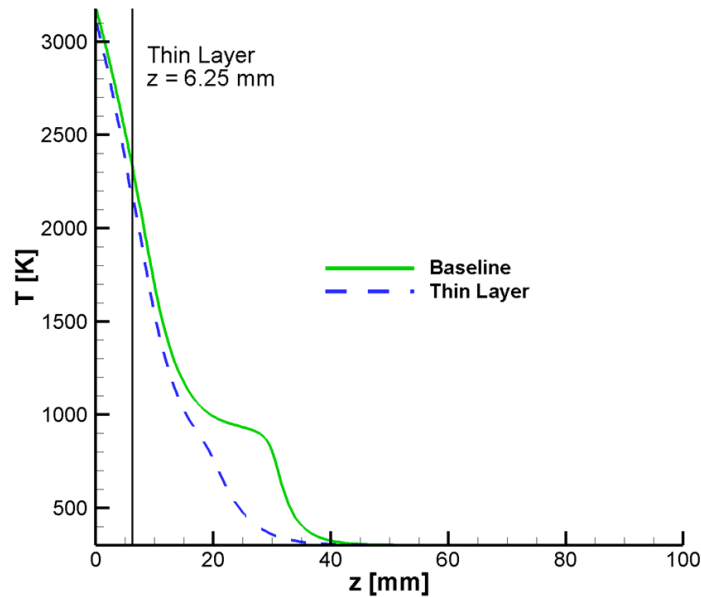


Figure 4.4: Temperature profiles for a 1D bar of TACOT material with and without a thin layer at  $t = 60\text{s}$ .

As mentioned earlier, this method introduced a discontinuity at the location of the thin layer due to the advective flux scheme applied. It is suspected that conservation of mass is not being observed in these cases for that reason. Since the velocity in the  $z$ -direction (Fig. 4.5a) has a large gradient across the thin layer the flux scheme thinks there is a shock in the material [53]. Figure 4.5b shows that the thin layer causes the gas in the material to stop being generated versus the typical uniform ablation seen in the baseline case. The peak is again shifted toward the heat surface indicating

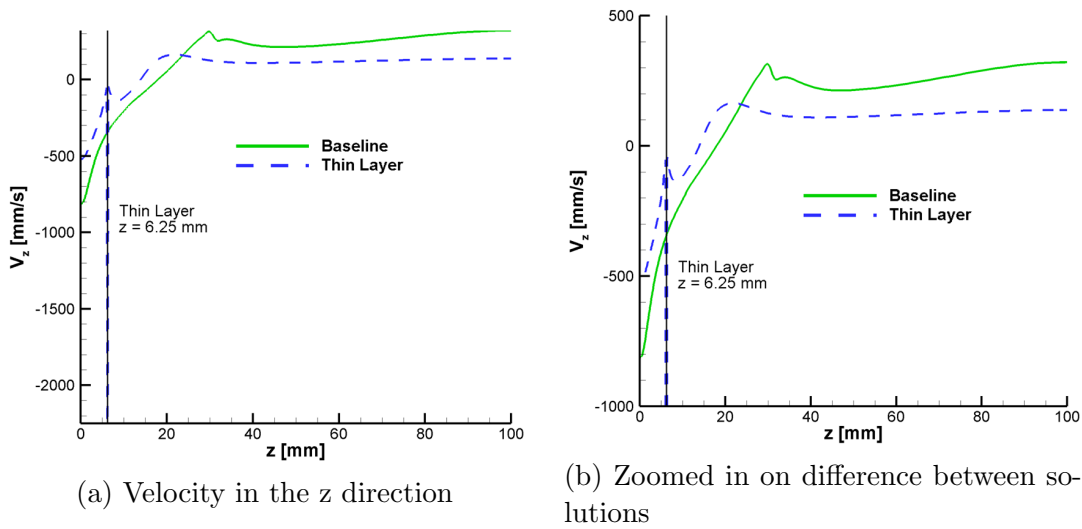


Figure 4.5: Velocity solution in the  $z$ -direction for 1D bar of TACOT with and without a thin layer.

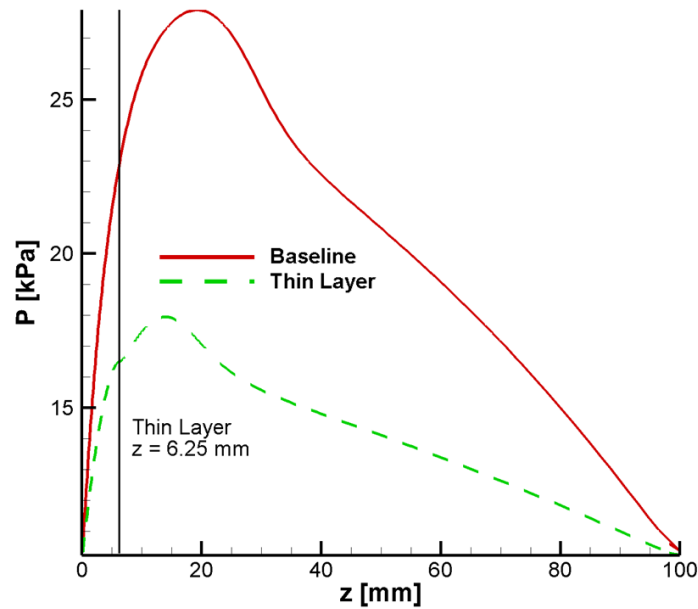


Figure 4.6: Pressure solutions for a 1D bar of TACOT with and without a thin layer at  $t = 60$  s.

that the thin layer presence in the material does affect the material behavior. The pressure profiles in Fig. 4.6 shows that there is a difference of 1000 Pa. The peak pressure shifts by 5 mm toward the heated surface of the material when the thin layer

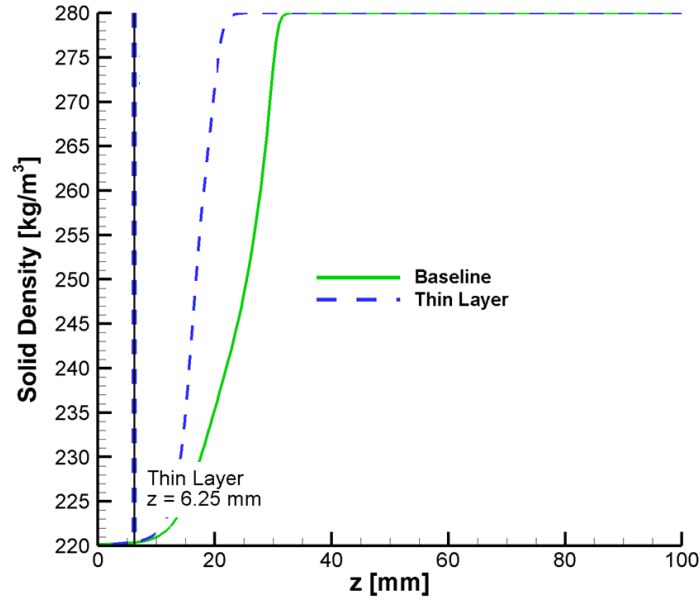


Figure 4.7: Solid density solutions for a 1D bar of TACOT material with and without a thin layer at  $t = 60$  s.

is present. This shift indicates that the thin layer does effect the gas behavior in the material when experiencing ablation. All of the material before the thin layer has been charred. The heat and thus ablation is being stopped by the thin layer. This leads to less pressure before the thin layer as there is not new gas being generated. The solid density represented in Fig. 4.7 provides more evidence that the thin layer does introduce a discontinuity in the material. It also provides further evidence that the thin layer slows down ablation. The solid density is the decomposition between the virgin and charred materials. Overall, in one dimension, the thin layer slows the process of ablation in the material.

## 4.2 Two Dimensional Charring Ablator

The next case studied was the two-dimensional flat plate. A constant thin layer was located at  $x = 5$  mm with  $1.83 \times 10^{-4}$  mm thickness. The material model used for the bulk properties is TACOT [48]. The thin layer material properties are shown in

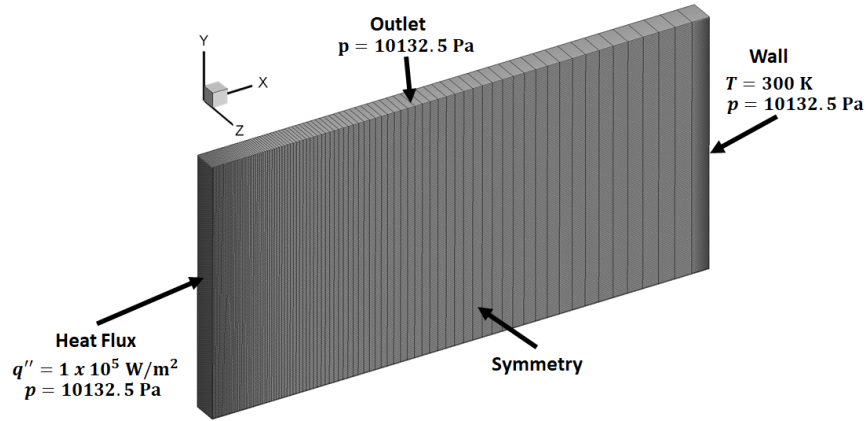


Figure 4.8: Computational domain for the 2D flat plate porous media case.

Table 4.1. The initial conditions for the flat plate were  $T = 300$  K and  $p = 10132.5$  Pa. The boundary conditions shown in Fig. 4.8 were used for the two-dimensional case and the computational domain consisted of  $200 \times 100$  cells with non-uniform spacing. A prescribed pressure boundary condition of  $p = 10132.5$  Pa was applied to the wall face, the face with the applied heat flux, and the outlet or free surface.

The centerlines were extracted at  $y = 5$  mm along the  $x$ -axis for both the baseline and thin layer case. Temperature and pressure profiles are plotted in Fig. 4.9a and Figure 4.9b respectively. The temperature profiles in Fig. 4.9a show that the thin layer sees less heat than the baseline case. The thin layer prevents the heat from reaching material after the thin layer which is needed to char the material and create pyrolysis gas. The front surface temperature is also lower but only by a few Kelvin. Figure 4.9b show the centerline pressure profiles. The thin layer pressure profile experiences a peak pressure of 10.53 kPa at  $x = 2$  mm. The baseline profile experiences a peak pressure of 11.32 kPa at  $x = 3$  mm. The difference between them is 790 Pa with a shift in the peak to the left in the thin layer case by 1 mm. As was seen in the one-dimensional case, the material to the right of the thin layer has not reached the temperature required for ablation. However, the pressure before the thin layer decreases as the gas has left the material from the front or top surfaces.

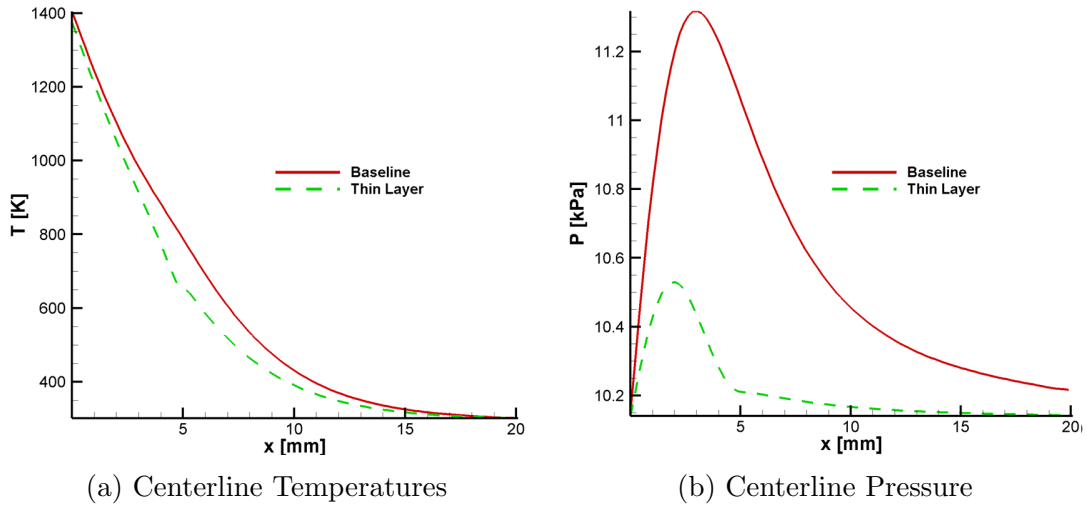


Figure 4.9: Extracted at centerline  $y = 5$  mm

The two-dimensional contours were plotted for each variable of interest. The first variable plotted in Fig. 4.10 is temperature. As was seen in the one dimensional case in the previous section, the temperature in the thin layer case was slower than in the baseline case. Both cases have the same overall behavior. The thin layer prevents the block of material from heating as quickly as the case without the thin layer present.

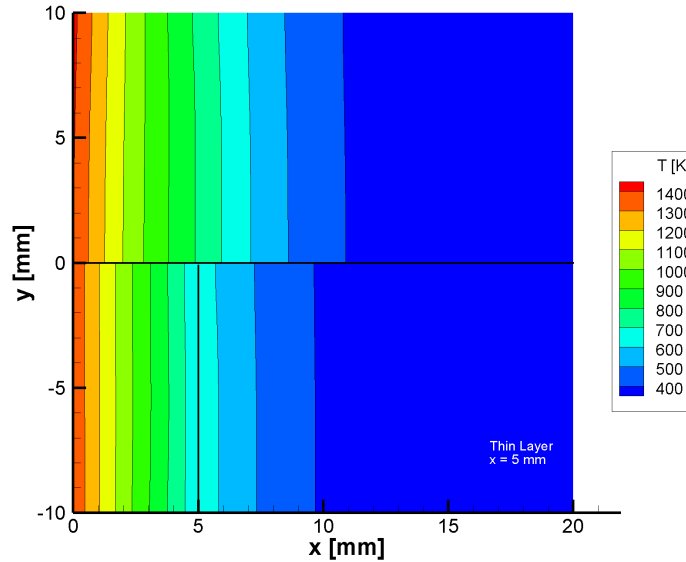


Figure 4.10: Temperature contours for baseline case without thin layer (top) and with a thin layer (bottom).

The next variable plotted is pressure. Figures 4.11 shows that the thin layer has a great effect on the pressure in the material. The curve in the pressure profile seen in the baseline case that is expected in ablation cases is not as developed when the thin layer is present. The pocket of pressure is both longer and thinner in the material when the thin layer is present versus when the thin layer is not. Fig. 4.11 shows that the curve in the pressure solution is not as dramatic. There is very little pressure built up behind the thin layer., while the pressure before the thin layer is lower due to the lack already being charred. The thin layer is preventing the pyrolysis gas generation by preventing heat from penetrating into the material. Meanwhile, the material in front of the thin layer has reached a state of char such that the majority of the gas has left the material through the open surfaces.

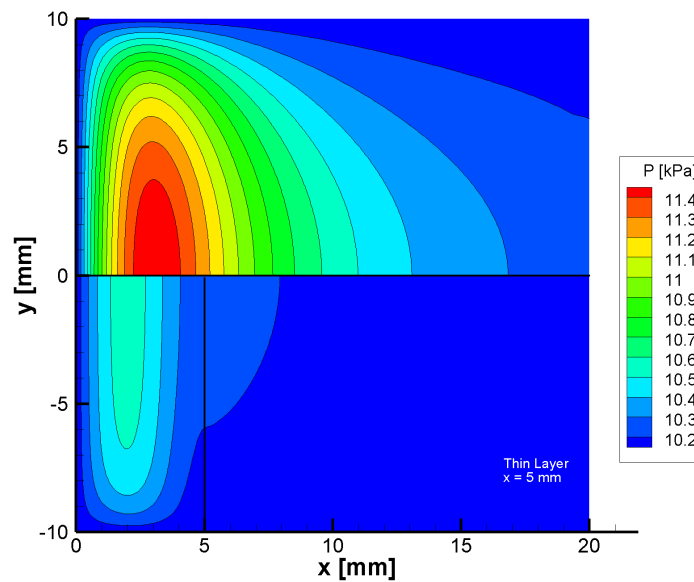


Figure 4.11: Pressure contours for baseline case without thin layer (top) and with a thin layer (bottom).

The solid density results are plotted in Fig. 4.12 for both the baseline and thin layer case. As seen in the one dimensional case, the thin layer ablates at a slower rate. There is also a large spike in solid density due to the massive difference in the material properties at the location of the thin layer. This is the darker red spot in

Fig. 4.12 is due to that discontinuity. It can also be seen that the ablation front had not made it to the thin layer; however, the presence of the thin layer does effect the behavior of the material.

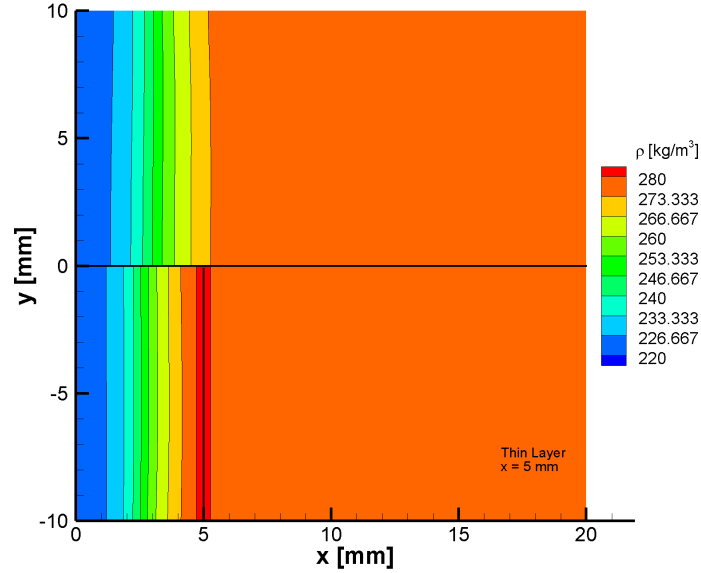
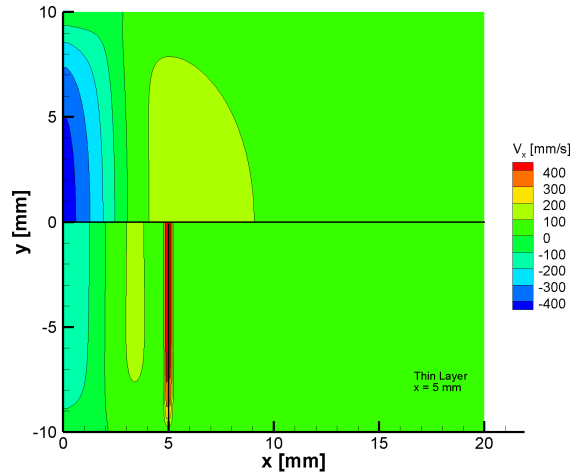


Figure 4.12: Solid density contours for baseline case without thin layer (top) and with a thin layer (bottom).

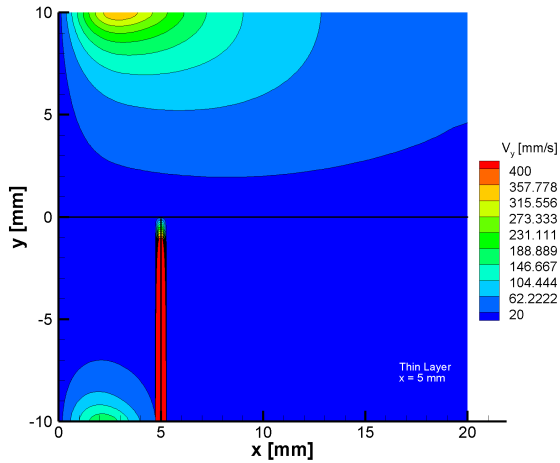
The velocity was analyzed in both the  $x$  and  $y$  directions and is shown in Fig. 4.13. The baseline case did have a velocity profile for both the  $x$  (Fig. 4.13a) and  $y$  (Fig.4.13b) direction when a material experiences ablation. The bulk of the gas exists out the side and front face of the material. However, when the thin layer is present the pressure, as previously discussed, is lower in the material which means the amount of gas is lower due to the lack of pyrolysis gas generation in the fully charred material. There is a spike in both the  $x$  and  $y$  direction in the thin layer.

The streamtraces for the velocity are plotted in Fig. 4.14. The gas is flowing in the material as expected in the baseline cases shown in Fig 4.14a and 4.14b. All the gas leaves from the free surfaces that was generated during ablation of that section of material through either the front surface or the top surface. The thin layer in the material slows pyrolysis gas generation and existing gas leaves the material. This is





(a) Velocity in the x direction contours



(b) Velocity in the y direction contours

Figure 4.13: Comparison between baseline case and thin layer case.

shown in Fig 4.14c and 4.14d.

Overall the presence of the thin layer matters when the material is experiencing ablation. However, the advective flux scheme caused mass to not be conserved in the material. The scheme treated the thin layer as a shock due to the large gradient in velocity and pressure. Their presence in a material prevents the material from ablating by preventing the heat from penetrating into the material. The material in front of the thin layer reaches a charred state, the gas leaves the material and no further gas is generated. This effects pressure and pyrolysis gas velocity in the

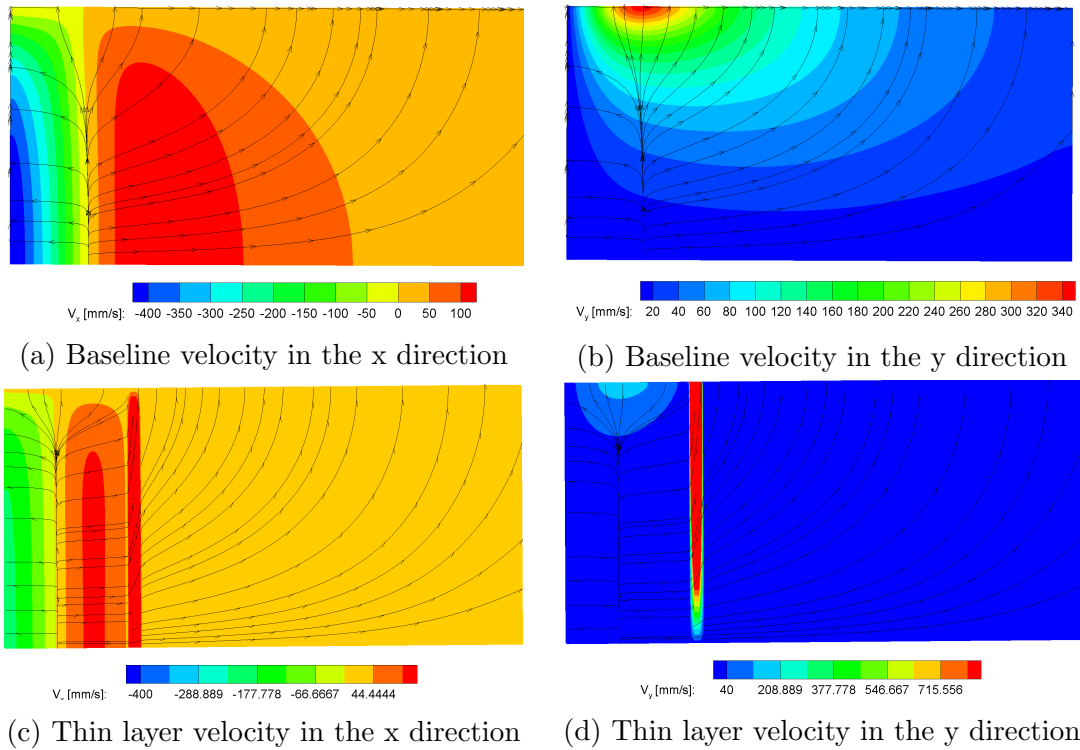


Figure 4.14: Plotted streamtraces for the baseline and thin layer cases.

material suggesting that thin layers can not be ignored. This method was able to capture the effect without the need to over resolve the computational domain.

## Chapter 5 Conclusion and Future Work

Vehicles used in extreme heat or oxygen rich environments require unique materials in order to withstand said conditions. These vehicles use TPS in order to ensure proper mission performance. One application that requires a TPS is when a vehicle is reentering the atmosphere of Earth. Thin layers of materials are used as one part of TPS. The manufacturing and application methods of thin layers in TPS have been studied for decades in experimental settings. However, little research has been done to study thin layers of materials for hypersonic applications and the effect they can have on the overall TPS behavior. State-of-the-art solvers need to resolve the computationally domain to the lowest dimension ( $\mu\text{m}$ ) while the TPS bulk material is on the order of cm. The over resolved domain is computationally expensive to run. Thus, most state-of-the-art solvers assume the thin layer has little effect and ignores their presence in the TPS. The material properties of the thin layer has also an order of magnitude different from the material properties of common TPS materials.

This work presented the volume-averaging flux-conservation method. The proposed method allows for the capture of the thin layer of material without the need to resolve the mesh to the lowest level of the thin layer by introducing a thin layer coefficient. The method was verified by testing a resolved method against a normal domain. The method was verified for the heat and diffusion equation. Then the method was applied to a one-dimensional bar, a two-dimensional bar, and two dimensional bars with non-uniform thin layer coefficients. The results showed that the method was able to capture a change in the overall behavior of the TPS when a thin layer is present. Finally the method was applied to a thin layer in an ablative material in a one-dimensional bar and a two-dimensional flat plate. The results showed that

the thin layer prevents the material from ablating thus, changing the behavior of the TPS.

This method will allow for the further study of thin layers of materials and their effects on the behavior of TPS. Thin layers can be made of SiC, which will melt when exposed to temperatures above 2000 K. This melted material could cause changes to the boundary layer composition as well as shape around the vehicle. Thus, a logical next step would be to incorporate the melting of the thin layer material. The method needs to be validated against experimental data. Once the method is validated, determining the sensitivity of the TPS behavior with the presence of a thin layer could be studied to better understand the effects at the macro scale, boundary layer and spallation of the material. Since this method in its implementation allows for each cell to be an average of material properties, it could be used to study localized defects in TPS. This would increase the understanding around the behavior of surface defects or localized pockets of impurities in materials as most surfaces are coating in thin layers of materials. Further investigation needs to be conducted to understand the conservation of mass issue noted in this work. According to Zhang [53], there is another advective flux scheme that should be applied when there is a large gradient in the velocity and pressure called AUSM-h. Moreover, further work should be conducted to determine the effects the thin layer has on ablation after the correct flux scheme is applied. It should also be noted that the material properties and heat are assumed to be isotropic. Therefore, a natural continuation of this work would be to consider anisotropic material properties and heating. This will allow for the testing of boundary cases in heat conduction to include a thin layer composed of air.

Copyright© Christen Setters, 2021

<https://orcid.org/0000-0003-2346-3713>

## Bibliography

- [1] Francioso, L., Presicce, D. S., Taurino, A. M., Rella, R., Siciliano, P., and Ficarella, A., “Automotive application of sol-gel TiO<sub>2</sub> thin film-based sensor for lambda measurement,” *Sensors and Actuators, B: Chemical*, Vol. 95, No. 1-3, 2003, pp. 66–72.
- [2] Akafuah, N. K., Poozesh, S., Salaimah, A., Patrick, G., Lawler, K., and Saito, K., “Evolution of the automotive body coating process-A review,” *Coatings*, Vol. 6, No. 2, 2016.
- [3] Zhang, J., France, P., Radomyselskiy, A., Datta, S., Zhao, J., and Van Ooij, W., “Hydrophobic cotton fabric coated by a thin nanoparticle plasma film,” *Journal of Applied Polymer Science*, Vol. 88, No. 6, 2003, pp. 1473–1481.
- [4] Dearnaley, G. and Arps, J. H., “Biomedical applications of diamond-like carbon (DLC) coatings: A review,” *Surface and Coatings Technology*, Vol. 200, No. 7, 2005, pp. 2518–2524.
- [5] Karki, S., Kim, H., Na, S. J., Shin, D., Jo, K., and Lee, J., “Thin films as an emerging platform for drug delivery,” *Asian Journal of Pharmaceutical Sciences*, Vol. 11, No. 5, 2016, pp. 559–574.
- [6] Hall, J., “Corrosion prevention and control programs for Boeing airplanes,” *SAE Technical Papers*, Vol. 102, 1993, pp. 161–170.
- [7] Miller, R. A., “Thermal barrier coatings for aircraft engines: History and directions,” *Journal of Thermal Spray Technology*, Vol. 6, No. 1, 1997, pp. 35–42.

- [8] Darolia, R., “Thermal barrier coatings technology: Critical review, progress update, remaining challenges and prospects,” *International Materials Reviews*, Vol. 58, No. 6, 2013, pp. 315–348.
- [9] Cao, X. Q., Vassen, R., and Stoeber, D., “Ceramic materials for thermal barrier coatings,” *Journal of the European Ceramic Society*, Vol. 24, No. 1, 2004, pp. 1–10.
- [10] Glass, D. E., “Ceramic matrix composite (CMC) thermal protection systems (TPS) and hot structures for hypersonic vehicles,” *15th AIAA International Space Planes and Hypersonic Systems and Technologies Conference*, , No. May, 2008, pp. 1–36.
- [11] Hurwitz, F., “Thermal Protection Systems,” *Encyclopedia of Aerospace Engineering*, chap. Thermal Pr, 2010, pp. 391–452.
- [12] Sziroczak, D. and Smith, H., “A review of design issues specific to hypersonic flight vehicles,” *Progress in Aerospace Sciences*, Vol. 84, 2016, pp. 1–28.
- [13] Bowman, W. H. and Lawrence, R. M., “Space Resource. Ablative Materials for High-Temperature Thermal Protection of Space Vehicles The,” *Journal of Chemical Education*, Vol. 48, No. 10, 1971, pp. 690.
- [14] Pavlosky, J. E. and St Leger, L. G., “Apollo experience report: Thermal protection subsystem,” *Apollo The International Magazine Of Art And Antiques*, , No. January 1974, 1974.
- [15] Uyanna, O. and Najafi, H., “Thermal protection systems for space vehicles: A review on technology development, current challenges and future prospects,” 2020.

- [16] Yang, Y. Z., Yang, J. L., and Fang, D. N., “Research progress on thermal protection materials and structures of hypersonic vehicles,” *Applied Mathematics and Mechanics (English Edition)*, Vol. 29, No. 1, 2008, pp. 51–60.
- [17] Blosser, M., Martin, C., Daryabeigi, K., and Poteet, C., “Reusable Metallic Thermal Protection Systems Development,” 1998.
- [18] Davuluri, R. S., Zhang, H., and Martin, A., “Numerical study of spallation phenomenon in an arc-jet environment,” *Journal of Thermophysics and Heat Transfer*, Vol. 30, No. 1, 2016, pp. 32–41.
- [19] Fahrenholtz, W. G. and Hilmas, G. E., “Ultra-high temperature ceramics: Materials for extreme environments,” *Scripta Materialia*, Vol. 129, 2017, pp. 94–99.
- [20] Wuchina, E., Opila, E., Opeka, M., Fahrenholtz, W., and Talmy, I., “UHTCs: Ultra-High Temperature Ceramic Materials for Extreme Environment Applications,” *The Electrochemical Society Interface*, Vol. 16, No. 4, 2007, pp. 30–36.
- [21] Chang, G. C., Phucharoen, W., and Miller, R. A., “Behavior of thermal barrier coatings for advanced gas turbine blades,” *Surface and Coatings Technology*, Vol. 30, No. 1, 1987, pp. 13–28.
- [22] Petrus, G. J. and Ferguson, B. L., “A software tool to design thermal barrier coatings: A technical note,” *Journal of Thermal Spray Technology*, Vol. 6, No. 1, 1997, pp. 29–34.
- [23] Freborg, A. M., Ferguson, B. L., Brindley, W. J., and Petrus, G. J., “Modeling oxidation induced stresses in thermal barrier coatings,” *Materials Science and Engineering A*, Vol. 245, No. 2, 1998, pp. 182–190.
- [24] Song, X., Meng, F., Kong, M., Wang, Y., Huang, L., Zheng, X., and Zeng, Y., “Thickness and microstructure characterization of TGO in thermal barrier coat-

- ings by 3D reconstruction,” *Materials Characterization*, Vol. 120, 2016, pp. 244–248.
- [25] Sheehan, J., Buesking, K., and Sullivan, B., “Carbon-carbon composites,” *Annual Review of Materials Science*, Vol. 24, No. 1, 1994, pp. 16–44.
- [26] Edie, D. D., “The effect of processing on the structure and properties of carbon fibers,” *Carbon*, Vol. 36, No. 4, 1998, pp. 345–362.
- [27] Károly, Z., Bartha, C., Mohai, I., Balázsi, C., Sajó, I. E., and Szépvölgyi, J., “Deposition of silicon carbide and nitride-based coatings by atmospheric plasma spraying,” *International Journal of Applied Ceramic Technology*, Vol. 10, No. 1, 2013, pp. 72–78.
- [28] Xu, B., Hong, C., Zhou, S., Han, J., and Zhang, X., “High-temperature erosion resistance of ZrB<sub>2</sub>-based ceramic coating for lightweight carbon/carbon composites under simulated atmospheric re-entry conditions by high frequency plasma wind tunnel test,” *Ceramics International*, Vol. 42, No. 8, 2016, pp. 9511–9518.
- [29] Corral, E. L. and Loehman, R. E., “Ultra-high-temperature ceramic coatings for oxidation protection of carbon-carbon composites,” *Journal of the American Ceramic Society*, Vol. 91, No. 5, 2008, pp. 1495–1502.
- [30] Jayaseelan, D. D., Xin, Y., Vandeperre, L., Brown, P., and Lee, W. E., “Development of multi-layered thermal protection system (TPS) for aerospace applications,” *Composites Part B: Engineering*, Vol. 79, 2015, pp. 392–405.
- [31] Smeacetto, F., Salvo, M., and Ferraris, M., “Oxidation protective multilayer coatings for carbon-carbon composites,” *Carbon*, Vol. 40, No. 4, 2002, pp. 583–587.



- [32] Friedrich, C., Gadow, R., and Speicher, M., “Protective multilayer coatings for carbon-carbon composites,” *Surface and Coatings Technology*, 2002.
- [33] Binner, J., Porter, M., Baker, B., Zou, J., Venkatachalam, V., Diaz, V. R., D’Angio, A., Ramanujam, P., Zhang, T., and Murthy, T. S., “Selection, processing, properties and applications of ultra-high temperature ceramic matrix composites, UHTCMCs—a review,” *International Materials Reviews*, Vol. 65, No. 7, 2020, pp. 389–444.
- [34] Hu, P., Cheng, Y., Wang, P., Guo, X., Ma, C., Qu, Q., Zhang, X., and Du, S., “Rolling compacted fabrication of carbon fiber reinforced ultra-high temperature ceramics with highly oriented architectures and exceptional mechanical feedback,” *Ceramics International*, Vol. 44, No. 12, 2018, pp. 14907–14912.
- [35] Heppenheimer, T. A., *Facing the Heat Barrier: A History of Hypersonics The Fading, the Comeback*, National Aeronautics and Space Administration, nasa histo ed., 2009.
- [36] Sutton, G. W., “Ablation of Reinforced Plastics in Supersonic Flow,” *Journal of the Aerospace Sciences*, Vol. 27, No. 5, 1960, pp. 377–385.
- [37] Bose, D., White, T., Santos, J. A., Feldman, J., Mahzari, M., Olson, M., and Laub, B., “Initial assessment of Mars Science Laboratory heatshield instrumentation and flight data,” *51st AIAA Aerospace Sciences Meeting including the New Horizons Forum and Aerospace Exposition 2013*, , No. January, 2013.
- [38] Beck, R. A., Driver, D. M., Wright, M. J., Hwang, H. H., Edquist, K. T., and Sepka, S. A., “Development of the mars science laboratory heatshield thermal protection system,” *Journal of Spacecraft and Rockets*, Vol. 51, No. 4, 2014, pp. 1139–1150.

- [39] Omidy, A. D., *Multiphase Interaction in Low Density Volumetric Charring Multiphase Interaction in Low Density Volumetric Charring Ablators Ablators*, Doctoral, University of Kentucky, 2018.
- [40] Szalai, C., Slimko, E., and Hoffman, P., “Mars science laboratory heatshield development, implementation, and lessons learned,” *Journal of Spacecraft and Rockets*, Vol. 51, No. 4, 2014, pp. 1167–1173.
- [41] Omidy, A. D., Panerai, F., Lachaud, J. R., Mansour, N. N., and Martin, A., “Effects of water phase change on the material response of low-density carbon-phenolic ablators,” *Journal of Thermophysics and Heat Transfer*, Vol. 30, No. 2, 2016, pp. 472–477.
- [42] Christiansen, E., Jim Arnold, U. o. C. a. S. C., Alan Davis, ESCG, N. J. S. C., James Hyde, ESCG, N. J. S. C., Dana Lear, N. J. S. C., J.-C. Liou, Ph.D., N. J. S. C., Frankel Lyons, ESCG, N. J. S. C., Thomas Prior, ESCG, N. J. S. C., Martin Ratliff, Ph.D., N. J. P. L., Shannon Ryan, Ph.D., L., Institute, P., Frank Giovane, V. T., Bob Corsaro, N. R. L., and George Studor, N. J. S. C., “Handbook for Designing MMOD Protection,” , No. June, 2009, pp. 64399.
- [43] Wright, W. W., “The effect of diffusion of water into epoxy resins and their carbon-fibre reinforced composites,” *Composites*, Vol. 12, No. 3, 1981, pp. 201–205.
- [44] Moyer, C. B. and Rindal, R. A., “An analysis of the coupled chemically reacting boundary layer and charring ablator. Part II: Finite difference solution for the in-depth response of charring materials considering surface chemical and energy balances,” 1968, pp. 168.

- [45] Amar, A. J., Oliver, B., Kirk, B. S., Salazar, G., Droba, J., Brandon Oliver, A., Kirk, B. S., Salazar, G., and Droba, J., “Overview of the charring ablator response (CHAR) code,” *46th AIAA Thermophysics Conference*, 2016, pp. 1–37.
- [46] Chen, Y. K. and Milos, F. S., “Multidimensional finite volume fully implicit ablation and thermal response code,” *Journal of Spacecraft and Rockets*, Vol. 55, No. 4, 2018, pp. 914–927.
- [47] Martin, A., Scalabrin, L. C., and Boyd, I. D., “High performance modeling of atmospheric re-entry vehicles,” *Journal of Physics: Conference Series*, Vol. 341, No. 1, 2012.
- [48] Weng, H., *Multidimensional Modeling of Pyrolysis Gas Transport Inside Charring Ablative Materials*, Ph.D. thesis, 2014.
- [49] Soloveichik, Y. G., Persova, M. G., Vagin, D. V., Epanchintseva, T. B., Dornikov, P. A., Dundukova, K. V., and Belov, V. K., “3D modeling of thermo-mechanical behavior of composite-made nose caps of hypersonic vehicle,” *Applied Thermal Engineering*, Vol. 99, 2016, pp. 1152–1164.
- [50] Ma, Y., Yao, X., Hao, W., Chen, L., and Fang, D., “Oxidation mechanism of ZrB<sub>2</sub>/SiC ceramics based on phase-field model,” *Composites Science and Technology*, Vol. 72, No. 10, 2012, pp. 1196–1202.
- [51] Düzel, Ü., Schroeder, O., Zhang, H., and Martin, A., “Computational prediction of NASA langley HYMETs arc jet flow with KATS,” *AIAA Aerospace Sciences Meeting, 2018*, No. 210059, 2018.
- [52] Fu, R., Weng, H., Wenk, J. F., and Martin, A., “Thermomechanical Coupling for Charring Ablators,” *Journal of Thermophysics and Heat Transfer*, 2017, pp. 1–11.

- [53] Zhang, H., *High temperature flow solver for aerothermodynamics problems*, Doctoral dissertation, University of Kentucky, 2015.
- [54] Li, Z., Zhang, H., Bailey, S. C., Hoagg, J. B., and Martin, A., “A data-driven adaptive Reynolds-averaged Navier–Stokes  $k$ – $\omega$  model for turbulent flow,” *Journal of Computational Physics*, Vol. 345, 2017, pp. 111–131.

# Christen Setters

[Christen.setters@us.af.mil](mailto:Christen.setters@us.af.mil) | 937.604.3914 | Centerville, OH

## Education

### **UNIVERSITY OF KENTUCKY | M.S. Mechanical Engineering**

Expected Grad Dec 2021

Concentration Computational Aerothermal Materials Fluids

**GPA: 3.73/4.0**

### **MIAMI UNIVERSITY | B.S. Physics**

Graduated May 2016

Minor in Mathematics | Dean's List - 2015 & 2016

**GPA: 3.5/4.0**

## DoD Experience

### **ALCMC/WISM | System Engineer & Digital Model/Architect**

Jan 2021 – Present

- Developed digital strategy for WISM
  - Helped to stand up DE environment for WIS programs
- Established cyber baseline for MC-130J ASSURANT
  - Projected to save 50% of rework time on subsequent ATO packages for xC-130J ATOs
- Digital engineering SME for AFSOC program
  - Coordinated access to environment; Tracked progress

### **AFMC Digital Campaign | Digital Engineer (LOEs #2,#3,#5)**

Feb 2020 – Present

- Developed digital strategy for outreach for the digital transformation
- Admin on MS Teams
  - helped manage users; data;
- Digital Guide Team
  - created the digital dictionary for the campaign
  - participated in creation of digital guide and contents
- Member of LOE2.4
  - helping revise contract language for ASDP and digital transformation
- Member of LOE 5.3
  - Contributed to training plan; took various training and provided feedback
- Member of LOE3.1 Team HiChew
- Mapped processes for the purposes for data tracing

### **AFLCMC/WAX | Program Integration System Engineer**

Aug 2019 – Jan 2021

- Coordinated PLM as lead product owner for F-15EX implementation of Teamcenter
  - Coordinated training, reviews, demos, messaging to leadership
  - Developed and conducted training to assist in the transition to telework as COVID response
  - Road mapped AF-PLM capability, developed messaging, tracked progress in Agile tools
- Lead digital transformation for Fighters and Bombers
  - Created educational content for digital transformation
  - Surveyed all F&B POs for status of digital; compiled results for leadership decision; road mapped digital transformation for F&B

## Experience

### Graduate Research Assistant | Gas Surface Interface Lab (GSIL)

May 2017 – Aug 2019

- Researched Kentucky Reentry Universal Payload System (KRUPS) using the Kentucky Aerothermal System (KATS) Computational Fluids Dynamics (CFD) Solver & KATS Material Response Solver (MR)
- Researched modeling thin layers of materials in KATS MR

### National Liaison | NASA Kentucky Space Grant

Aug 2016 – May 2017

- Coordinated with schools across the nation for the Eclipse Ballooning Project
- Responsible for reporting to organizing institution on progress & outcomes, practice launches, team meetings via written reports & Telecommunications

### Undergraduate Assistant | Miami University Physics Department

Jan 2013 – June 2016

- Managed inventory and equipment for undergraduate physics labs
- Created & implemented a standard documentation (videos & written instructions) for equipment use & classroom instruction
- Assisted professors & teaching assistants with teaching physics experiments to students

### Undergraduate Researcher | Computational Physics Lab

May 2015-May 2016

- Developed a simulation with a MATLAB Guided User Interface(GUI) for an optical lattice

### Logistics Coordinator | Miami University Physics Department

May 2014 – Aug 2014

- Developed & implemented logistics plans for moving research & teaching lab equipment

## Skills

**Programing:** Bash, MATLAB, Python, LATEX, C++, Fortran, Inventor, Arduino, LabView, SysML

**DE Tools:** Teamcenter, Cameo, ASSURANT, Rapsody

**Lab Equipment:** Oscilloscope, Soldering, High Voltage Power Supplies, Multi-meter, Drill Press, Band Saw

**Certificates:** Computational Fluid Dynamics Graduate Certificate, DAU ENG Lvl I

## Awards & Leadership

2016 - Present	Graduate Mechanical Engineering Student Panelist & Volunteer
Aug 2017 - Present	Research Assistant for GSIL
Dec 2018	1st Place ME Poster Competition
2014 – 2016	Vice President/President SPS at Miami University
2015 - 2016	Math & Physics Tutor for the Naval ROTC Program
May 2015 - Aug 2015	Undergraduate Research Scholar at Miami University

## Relevant Coursework

Advanced Electronics	Advanced Combustion	Computational Physics
Material Physics	Gas Dynamics	Mathematical Methods in Physics
Turbulence	In-compressible CFD	Applied Mathematical Modeling
Numerical Methods	Applied Nonlinear Dynamics	Leadership Theory
Partial Differential Equations	Quantum Mechanics	

References available upon request.